Synthesis and Characterization of Model Compounds for Self-Assembled Dithienophosphole-Based Phosphinamides

Mary Odagwe

A thesis submitted to the Faculty of Graduate Studies in partial fulfilment of the requirements for the degree of Master of Chemistry

Department of Chemistry, York University

Toronto, Canada

August 2025

Abstract

On the path to synthesizing classes of dithienophosphole soft materials, this thesis documents the synthesis and characterization of model compounds for self-assembled dithienophosphole-based phosphinamides. Expanding upon the blue-emitting series within this class of compounds and targeting applications in white OLEDs, green and orange emitters, along with their corresponding model compounds, are reported. Taking advantage of the ease of functionalizing the α-position of the dithienophosphole core, the emitter compounds were synthesized via Suzuki cross-coupling reactions. The model compounds, incorporating hydrogen-bonding moieties, were prepared through substitution at the phosphorus center. Comprehensive characterization was performed, including optical and spectroscopic analyses, and full synthetic details are provided.

Acknowledgements

I want to begin by expressing my deepest gratitude to my supervisor, Dr. Thomas Baumgartner, who took a chance on me since my undergraduate days. I thank him for his ongoing support, invaluable guidance, encouragement, and for providing a safe, comfortable workspace. I also appreciate my committee members, Dr. Ryan Hili and Dr. Christopher Caputo, for their support, insightful feedback, and collaboration. I am forever grateful to my family in Calgary and friends, both new and old, for their encouragement, support, and patience through the tears and during the most challenging times of my journey. I want to extend my thanks to members of the Baumgartner group, past and present, for their help and feedback. Special thanks to Farnaz, Samira, Reza, and Taylor, who offered daily support, advice, crash courses, and expertise that greatly contributed to my work. Thank you to the Caputo and Hili groups, as well as everyone in the department, including the instrumentation and administration staff, for their contributions to my journey. Thank you to NSERC for their funding. Last but not least, I want to thank God: Father, I thank thee.

Table of Contents

List of Tables

List of Figures

List of Schemes

List of Abbreviations and Symbols

Abs	Absorption
AIEE	Aggregation-Induced Enhanced Emission
CIE	Commission Internationale de l'Éclairage
DFT	Density Functional Theory
DNA	Deoxyribonucleic Acid
ε	Extinction Coefficient
Em	Emission
EML	Emissive Layer
ETL	Electron Transport Layer
eV	electron Volts
FRET	Fluorescence/Förster Resonance Energy Transfer
HIL	Hole Injection Layer
HOMO	Highest Occupied Molecular Orbital
HTL	Hole Transport Layer
ICT	Intramolecular Charge Transfer
ITO	Indium tin oxide
LCs	Liquid Crystals
LUMO	Lowest Unoccupied Molecular Orbital
NBS	N-bromosuccinimide
OFETs	Organic Field Effect Transistors
OLEDs	Organic Light Emitting Diodes
OPVs	Organic Photovoltaics
PLQY	Photoluminescence Quantum Yield
POM	Polarized Optical Microscopy
ppm	part per million

SmA	Smectic-A
SmC	Smectic-C
TADF	Thermally-Activated Delayed Fluorescence
TD-DFT	Time-Dependent Density Functional Theory
TLC	Thin-Layer Chromatography
UHD	Ultra-High-Definition
WOLEDs	White OLEDs

Chapter One: Introduction

1.1 Organic π-Conjugated Materials

Extensive research has been directed toward developing alternatives to metal-based materials in pursuit of sustainable and environmentally benign technologies. Among these, organic π-conjugated materials have emerged as a particularly promising class, attracting significant attention for their potential in optoelectronic, photonic, energy, and sensing applications, where they offer a viable substitute for conventional silicon- and metal-based systems. These materials not only exhibit lower toxicity and reduced environmental impact but also benefit from cost-effective manufacturing processes. Their compatibility with solution-based techniques, such as spin-coating, facilitates facile integration onto a variety of substrates. A key advantage of π-conjugated systems lies in their structural tunability at the molecular level, enabling precise modulation of their electronic and optical properties.[1] Through this path, researchers are continuously developing new organic conjugated materials with better performance, and stability for applications such as organic photovoltaics (OPVs), organic light emitting diodes (OLEDs), and organic field effect transistors (OFETs).[1,2]

The unique electronic properties of organic π-conjugated materials arise from their characteristic structure, in which alternating single and double bonds facilitate the delocalization of π-electrons across the conjugated backbone. This delocalization results in the formation of extended molecular orbitals that span the entire conjugated system, effectively reducing the energy required for electron excitation. The extent of conjugation directly influences the electronic structure, particularly the energy levels of the highest

occupied molecular orbital (HOMO) and the lowest unoccupied molecular orbital (LUMO). The HOMO-LUMO band gap can be tuned by varying the degree of conjugation, through structural modifications of altering the length of the conjugated chain or incorporating functional groups. This tunability is crucial for tailoring the optical and electronic properties of the material, enabling precise control over fundamental characteristics such as light absorption and emission spectra, and charge transport properties.[3]

Depending on the energy difference in the band gap of a material, it can be classified into a conductor, a semiconductor, or an insulator. The valence and the conduction band are also known as HOMO and LUMO in molecular species, respectively. Conductors, such as metals, have either no band gap or overlapping valence and conduction bands, allowing free movement of electrons under an applied electric field. Insulators, on the other hand, possess wide band gaps (typically >3 eV), which prevent significant electron flow under normal conditions. Organic π-conjugated materials occupy an intermediate position, functioning as semiconductors due to their moderate band gaps, generally ranging from approximately 1.4 eV to 3 eV. While the delocalization of these materials facilitates charge mobility, it does not eliminate the energy gap between the HOMO and the LUMO. As a result, organic π-conjugated materials cannot conduct electricity as freely as metals. The Band Theory, illustrated in Figure 1-1, explains how electronic conduction arises in these materials. When many molecules aggregate, the discrete energy levels of individual molecular orbitals broaden into energy bands due to intermolecular interactions. Depending on the alignment and overlap of these molecular orbitals, charge carriers (electrons or holes) can move through the material under an

applied voltage, making them suitable for use in electronic and optoelectronic applications such as OLEDs.[4,5]

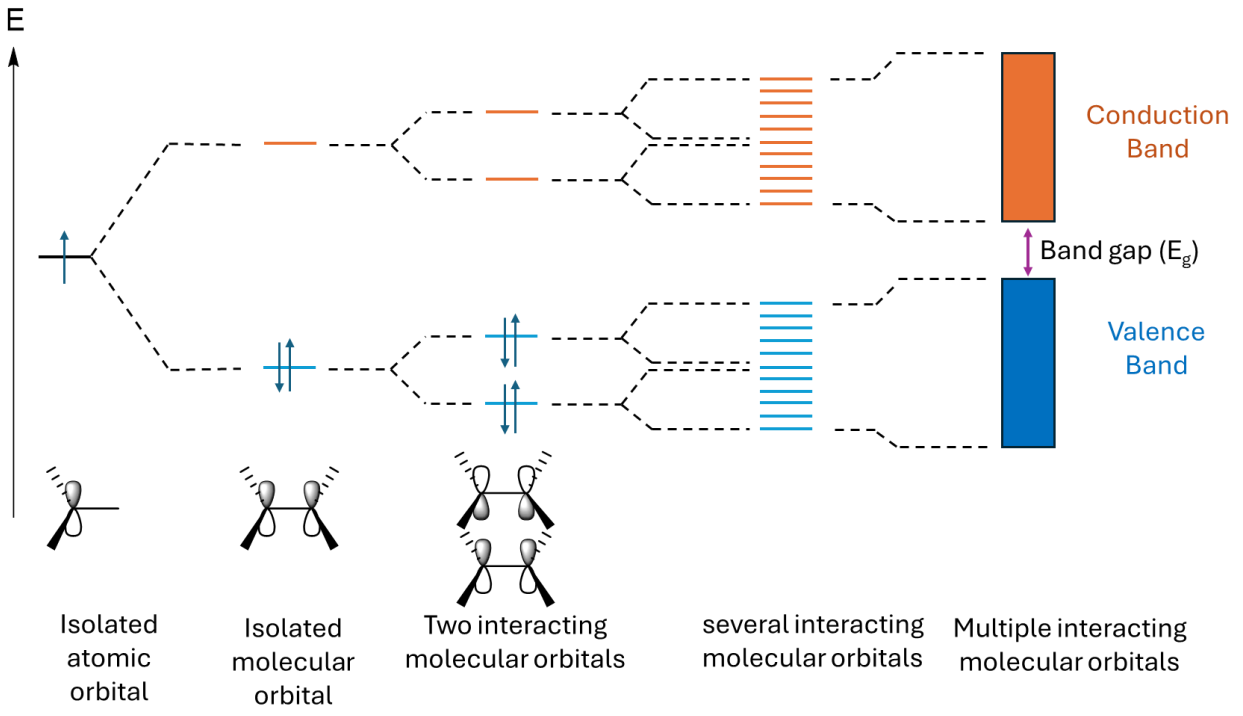

Figure 1-1: Interaction of molecular orbitals, giving rise to the conductivity of organic π-conjugated materials

1.1.1 OLEDs

The luminescence of organic π-conjugated materials makes them particularly valuable for performance in optoelectronics such as OLEDs. OLEDs are a recently developed display technology that has gained traction for offering several key advantages, including high energy efficiency, vibrant color reproduction, excellent contrast, wide viewing angle, flexibility, etc. They also have the added benefit of mercury-free

manufacturing, making them more environmentally friendly than older technologies. They also eliminate the need for backlighting, which is typically used in LED and incandescent lighting. This innovative display technology has moved beyond the lab and into the consumer market, where it now plays a central role in a wide range of electronic devices. OLEDs are found in digital cameras, smartphones, smartwatches, and ultra-high-definition (UHD) televisions, offering users a visually rich and immersive experience. With continued research and development, OLEDs are also paving the way for flexible, foldable, and even transparent displays, broadening their potential in next-generation electronics.[6]

The working principle of OLEDs is electroluminescence, a process in which the application of an external voltage leads to the generation of excitons, bound electron-hole pairs in an excited state. These excitons subsequently undergo radiative recombination, resulting in photon emission. A typical OLED architecture (Figure 1-2) consists of several key components: a substrate that provides mechanical support, a transparent anode (often indium tin oxide, ITO), a series of organic layers, including emissive and charge-transport materials, and a cathode. The essential functional components of the electroluminescent mechanism reside within the organic layer stack (Figure 1-2), which is typically divided into three major sub-layers: the hole injection/transport layer (HIL/HTL), the emissive layer (EML), and the electron-transport layer (ETL). The HIL/HTL facilitates the injection and transport of holes from the anode into the valence band of the emissive material. Simultaneously, the ETL enhances the injection and mobility of electrons from the cathode into the conduction band of the emissive layer. Within the emissive layer, electrons and holes recombine to form excitons, which decay radiatively to emit light. The

emitted wavelength, and thus the perceived color, corresponds to the band gap of the emissive material used.[6–8]

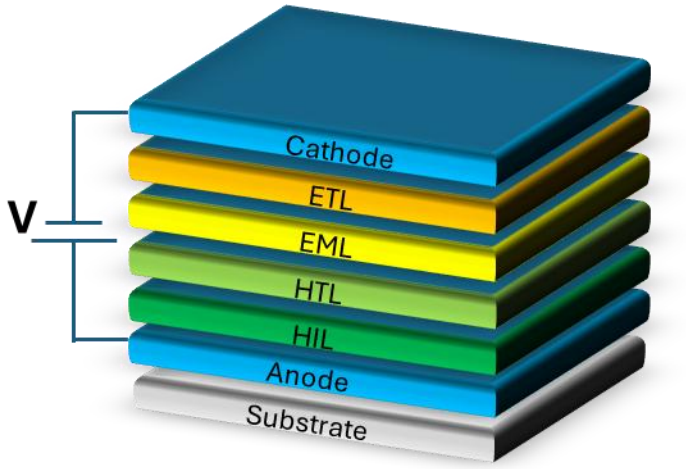

Figure 1-2: Typical OLED architecture.

A specific class of OLEDs are White OLEDs (WOLEDs) that are designed to emit a continuous and broad spectrum of white light. This design offers several advantages, including uniform, full-spectrum illumination, and the capability to fabricate large-area panels suitable for applications such as indoor lighting. Objects that are illuminated by WOLEDs appear more accurately colored and natural. Additionally, WOLEDs present the potential for reduced power consumption compared to conventional OLED systems, particularly when optimized for high luminous efficacy across wide emission areas. White light emission can be achieved through the appropriate combination of primary colors, red, green, and blue, or by blending complementary emitters such as orange and blue. The quality and accuracy of the resulting white light are typically assessed using the Commission Internationale de l'Éclairage (CIE) chromaticity coordinates. An ideal white

light corresponds to a CIE coordinate of (0.33, 0.33), representing balanced emission across the visible spectrum (Figure 1-3).[9]

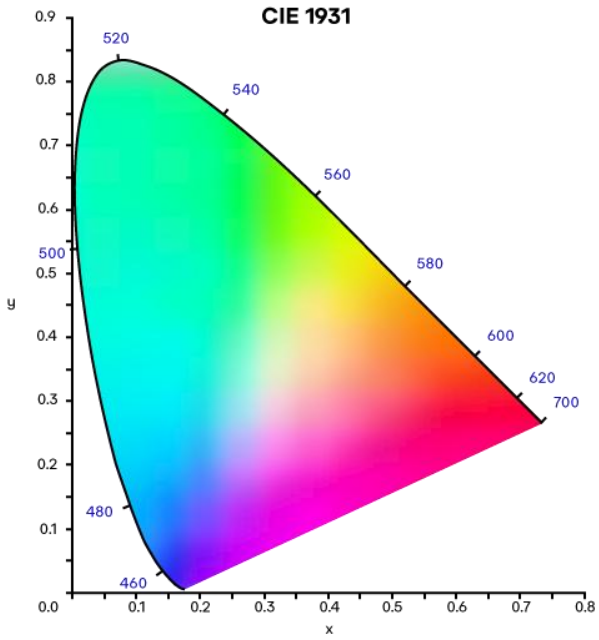

Figure 1-3: CIE 1931 color space chromaticity diagram used to assess white light emission.[10]

The organic π-conjugated emitters in WOLEDs are employed in either stacked or blended configurations to produce white light emission (Figure 1-4). Blended WOLEDs, which incorporate multiple emitters within a single emissive layer, offer advantages in fabrication simplicity. However, they are often hindered by issues such as phase separation, exciton quenching, and differential degradation rates among the constituent emitters, all of which can compromise device stability and color uniformity over time.[9] To overcome these limitations, ongoing research is focused on the development of stable organic π-conjugated materials capable of intrinsically emitting across multiple spectral

regions. These materials feature integrated molecular frameworks that resist phase separation and degradation while simultaneously enabling broadband emission, thereby offering a promising pathway toward more reliable and efficient WOLEDs.[11,12]

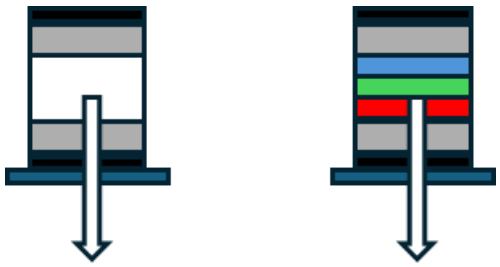

Figure 1-4: Example of a blended and stacked WOLED device.

1.1.2 Organic π-Conjugated Materials in OLED Emissive Layers

Emission in organic materials occurs through mechanisms of photoluminescence, primarily including fluorescence, phosphorescence, and thermally-activated delayed fluorescence (TADF). Fluorescence involves the radiative decay of an excited singlet state to the ground state, maintaining the spin multiplicity. In contrast, phosphorescence arises from a spin-forbidden transition, typically involving intersystem crossing from an excited triplet state to a singlet ground state, which results in longer-lived emission. TADF represents a specific case of delayed fluorescence in which triplet excitons are thermally upconverted to the singlet state, followed by radiative emission.[13] This mechanism effectively harnesses triplet excitons for fluorescence and is particularly valuable in OLED technologies for enhancing efficiency.

The EML sublayer is a critical component of an OLED device, since it is the region where electroluminescence occurs, making it essential for the device's functionality and overall performance. Without this layer, the device cannot emit, therefore, it serves no practical

purpose. Hence, while organic π-conjugated materials can be incorporated into various sublayers of the device, such as the HIL/HTL and the ETL, their role in the EML is of particular importance.[8] Organic π-conjugated materials used in the EML of OLEDs are specifically engineered to emit light in the red, green, blue, or orange regions of the visible spectrum (Figure 1-5). The primary classes of these emissive materials include small molecules, conjugated polymers, and conjugated dendrimers, each offering unique structural and optoelectronic advantages. Representative blue emitters include carbazole derivatives, anthracene-based compounds, and polyfluorene polymers, all of which exhibit high-energy emission and favorable thermal and photostability. Green emission is typically achieved using silole-based materials and coumarin-derived dopants, both known for their high quantum yields and efficient charge transport properties. For red emission, commonly used materials include phenothiazine derivatives and polythiophene-based conjugated systems, which provide deep-red emission, good film-forming properties, and structural versatility. [8,14,15]

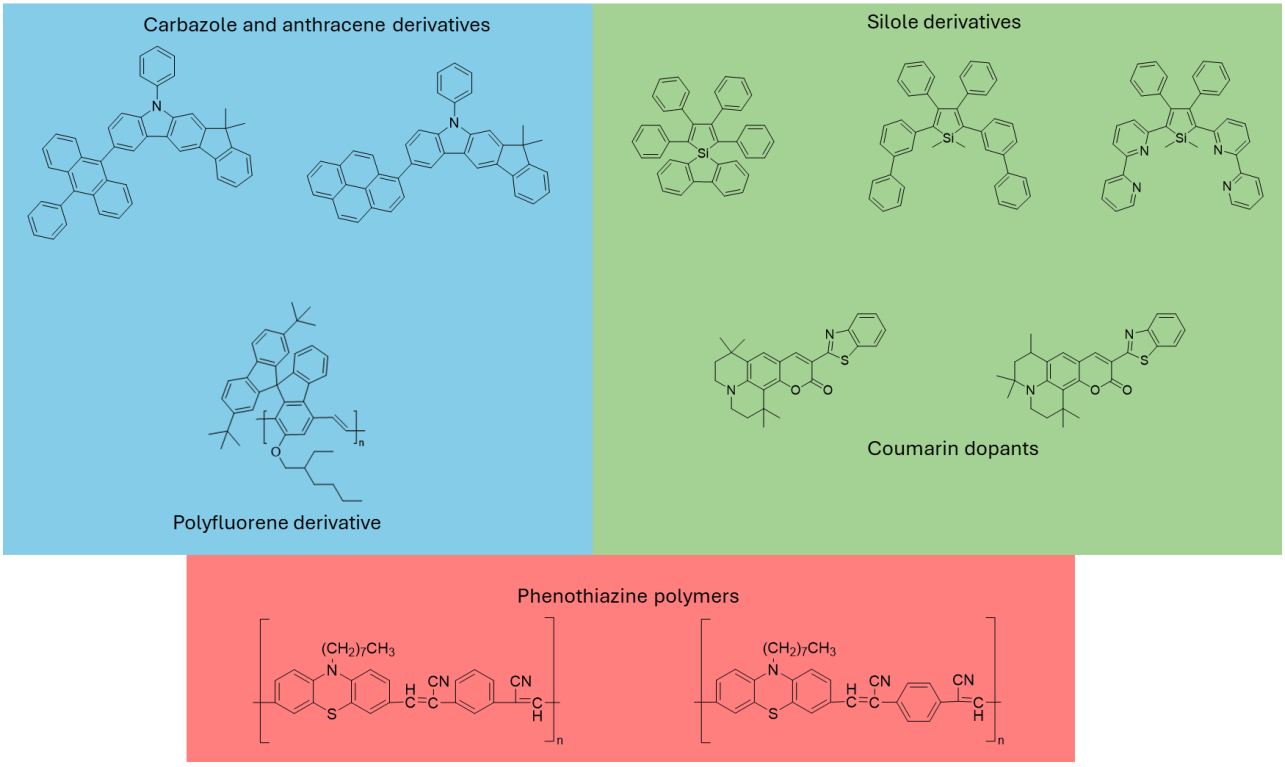

Figure 1-5: Representative organic emitters for EMLs in OLEDs.

1.2 Molecular Self-Assembly

One effective strategy to minimize phase separation and promote synergistic interactions between organic emitters is through molecular self-assembly. Molecular self-assembly refers to the spontaneous organization of discrete molecular components into ordered, higher-order structures, often resulting in emergent functional properties. In such systems, individual building blocks organize autonomously, without the need for external guidance or templating. Non-covalent interactions, including van der Waals forces, electrostatic interactions, coordination, and hydrogen bonding typically govern this process. Self-assembly can occur either intermolecularly, involving associations between

identical monomers or different molecular species, or intramolecularly, as seen in the folding behavior of macromolecules such as peptides or conjugated polymers. Through careful molecular design, self-assembly can be harnessed to create structures with enhanced optoelectronic properties, stability, and charge transport characteristics.[16,17]

Many researchers have turned to nature for inspiration in synthesis,[18,19] and molecular self-assembly is no exception. Self-assembly is also a fundamental biological process inherent to all living organisms, playing a central role in the formation of complex structures. Key examples include the spontaneous formation of lipid bilayers, micelles, protein folding, and the double helical structure of deoxyribonucleic acid (DNA), all driven by non-covalent interactions such as hydrogen bonding and electrostatic forces. Nature also demonstrates how self-assembly can introduce new functionality, as seen in the formation of secondary protein structures (Figure 1-6). The distinction between α-helices and β-sheets arises solely from differences in hydrogen bonding patterns between amino acid residues. This naturally occurring phenomenon has become increasingly valuable in materials science.[20]

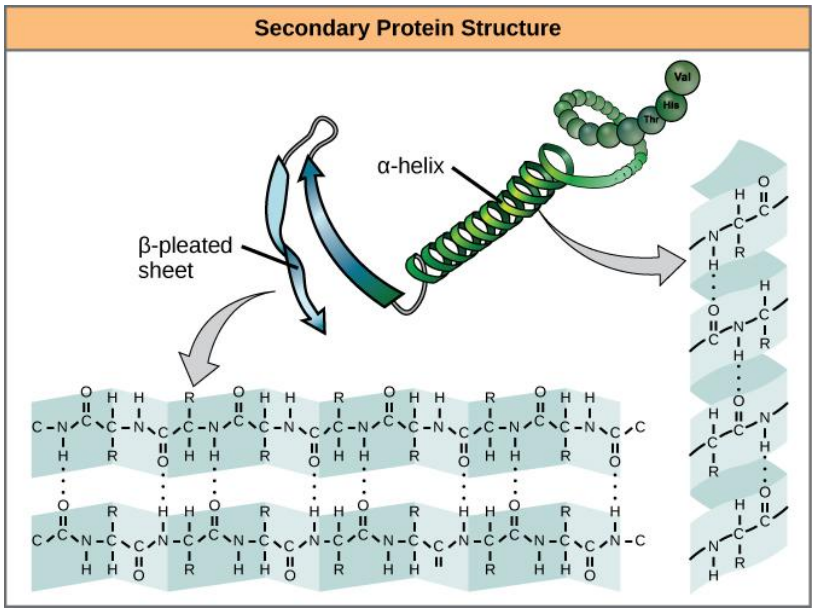

Figure 1-6: Formation of secondary protein structures through hydrogen bonding.

Molecular self-assembly represents a highly versatile and efficient phenomenon for the organization of organic soft materials into well-defined, functional systems. This bottom-up approach enables the formation of self-assembled organic systems that have found broad utility across numerous technological domains, including molecular sieving, microfabrication, bio-membranes, chemical sensing, display technologies, and optoelectronics.[17] In parallel, organogels and hydrogels, owing to their dynamic, responsive networks, are increasingly utilized in stimuli-responsive systems.[21,22] The ability of these materials to self-organize into hierarchical architectures continues to expand the design space for next-generation functional materials.

Liquid crystals

Liquid crystals (LCs) are a distinct class of soft materials that exhibit intermediate properties between those of conventional liquids and crystalline solids. Their degree of molecular order, which determines the extent of long-range orientational and positional alignment, is a key factor influencing their mesomorphic behavior and optical characteristics. Due to their intrinsic anisotropy, LCs are commonly characterized using polarized optical microscopy (POM), which enables observation of their intriguing textures. Liquid crystals are broadly classified into two primary mesophases: lyotropic and thermotropic. The lyotropic liquid crystals consist of two or more components that display liquid-crystalline properties within certain concentration ranges. Thermotropic LCs exhibit phase transitions in response to temperature changes and include several well-defined phases such as nematic, smectic-A, smectic-C, cholesteric (chiral nematic), and discotic mesophases, each with distinct structural organization and physical properties (Figure 1-7).[23,24]

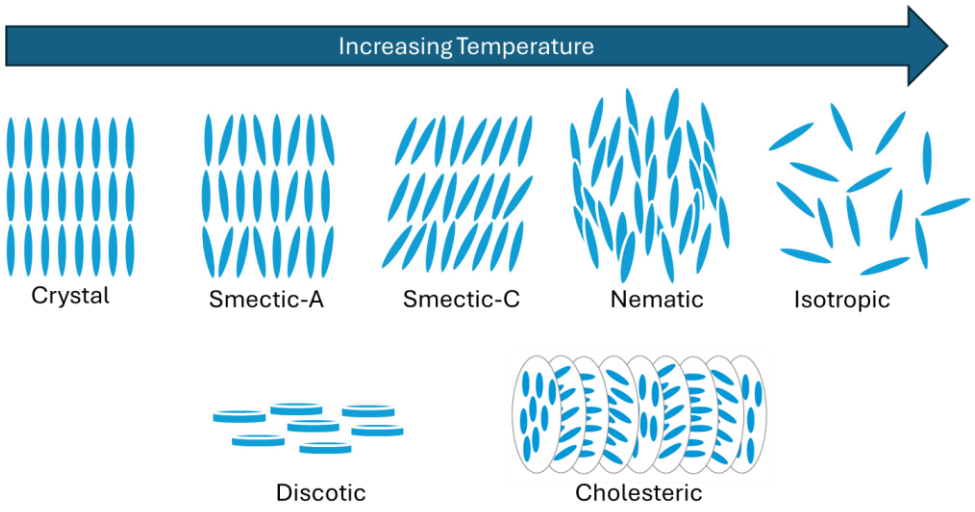

Figure 1-7: Liquid crystal thermotropic mesophases.

In the nematic phase, molecules exhibit long-range orientational order but lack any positional ordering. That is, while the molecular long axes tend to align along a common direction, defined by the director, the centers of mass of the molecules remain randomly distributed, akin to a liquid. In the smectic-A (SmA) phase, molecules maintain the orientational order of the nematic phase but also organize into well-defined layers, with their long axes perpendicular to the layer planes. The smectic-C (SmC) phase also features a layered structure, but with a key distinction: the molecular axes are tilted with respect to the layer normal due to their chirality. The cholesteric phase, also known as the chiral nematic phase, is a variant of the nematic mesophase in which the molecules are chiral. As a result of this chirality, the director rotates in a helical fashion along an axis perpendicular to the molecular alignment, forming a helical superstructure. The discotic mesophase is composed of disk-shaped mesogens, planar, often aromatic molecules capable of forming liquid crystalline phases.[23–25]

Organogels

A gel is a semisolid material made up of a three-dimensional network of either colloidal or polymeric structures that are swollen by and entrap a substantial quantity of liquid within their matrix. Organogels are a special class of gels where both the gelator, a compound capable of forming a gel, and the fluid phase are organic (Figure 1-8). The formation of organogel follows a molecular self-assembly mechanism through interactions such as hydrogen bonding, π–π stacking, van der Waals forces, or hydrophobic interactions to form a fibrous or lamellar framework that immobilizes the

surrounding organic solvent. Organogels can retain up to 99% of the solvent phase while maintaining a stable, solid-like structure. They are capable of retaining up to 99% of the liquid phase, absorbing and releasing various substances, and exhibiting stimuli-responsive behavior to a range of external triggers, including temperature, light, pH, and mechanical deformation.[22]

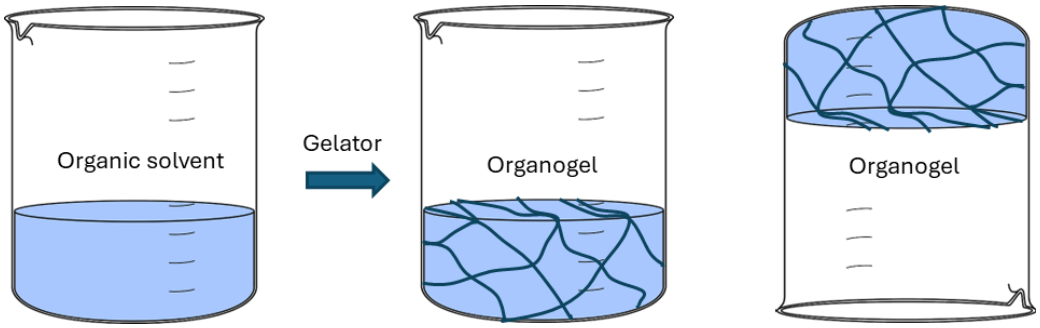

Figure 1-8: Depiction of gelator assembling into a 3D network to form an organogel.

1.2.1 Self-Assembled Organic π-Conjugated Materials in OLED Emissive Layers

The organic emitters discussed earlier exhibit varying degrees of self-assembly, primarily driven by non-covalent interactions such as van der Waals forces and π–π stacking. These interactions play a role in determining the solid-state packing and optoelectronic properties of the materials. Derivatives of compounds mentioned above such as anthracene and carbazole can also form self-assembled emissive structures. Beyond these small-molecule derivatives, more complex architectures have also been explored to harness self-assembly for functional optoelectronic materials. For instance, discotic liquid crystalline emitters can form columnar mesophases that facilitate anisotropic charge transport and stable emission behavior. Similarly, dendritic emitters

featuring branched, tree-like molecular frameworks have been synthesized to control intermolecular interactions and suppress aggregation-induced quenching (Figure 1-9).[26–28]

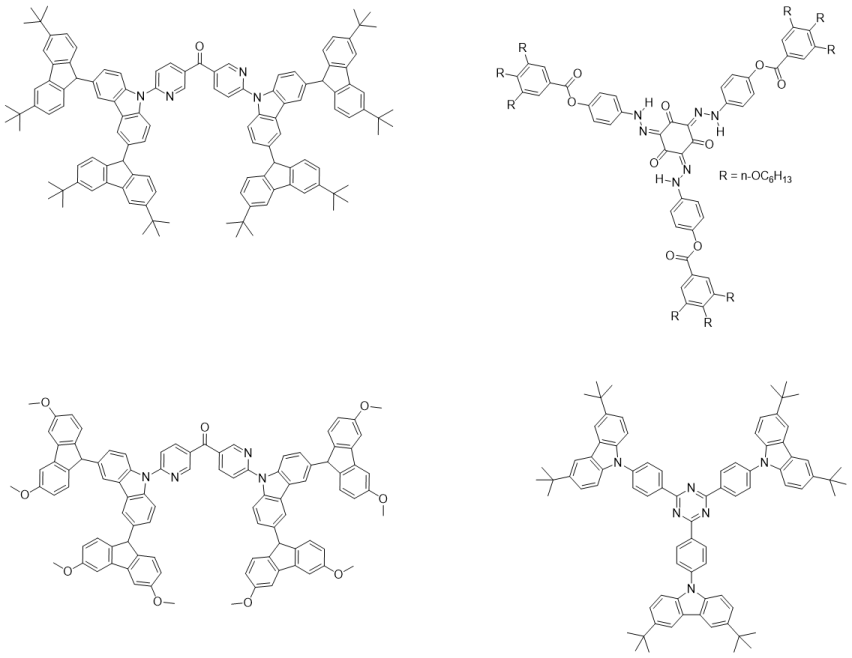

Figure 1-9: Examples of dendritic and discotic emitters.

1.3 Phospholes

Phospholes are a class of five-membered phosphorus-containing heterocycles. Compared to pyrroles, they exhibit only weak aromaticity due to the limited interaction between the lone pair on the phosphorus atom and the adjacent butadiene moiety. They are pyramidal while pyrroles are planar. However, this reduced aromatic character is not a drawback; rather, it enhances the reactivity and ease of functionalization at the phosphorus center. The partial localization of electron density within the ring makes

phospholes particularly well-suited for tuning electronic properties through structural modification, especially in extended π-conjugated systems.[29]

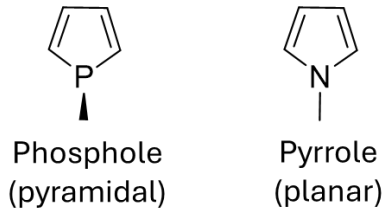

Figure 1-10: The structural distinction between phosphole and pyrrole lies primarily in the nature of the heteroatom and its electronic interactions with the conjugated system.

1.3.1 Dithieno[3,2-*b*:2',3'-*d*]phosphole Materials

Dithienophospholes are a class of π-conjugated organic materials that have been extensively studied by the Baumgartner group for their multifunctional properties. Structurally, they comprise a phosphole core fused to two thiophene rings, incorporating both phosphorus and sulfur heteroatoms, elements that impart unique electronic characteristics (Figure 1-11). These compounds have shown significant potential for a variety of organic electronic applications, including OLEDs, organic field-effect transistors (OFETs), and chemical sensors. The electronic and photophysical properties of dithienophospholes can be finely tuned through modifications to the conjugated backbone or substitutions at the phosphorus center, enabling the design of versatile functional materials. Notably, certain derivatives can be engineered to self-assemble into liquid

crystalline phases or organogels, offering enhanced optoelectronic performance and responsiveness to stimuli.[30,31]

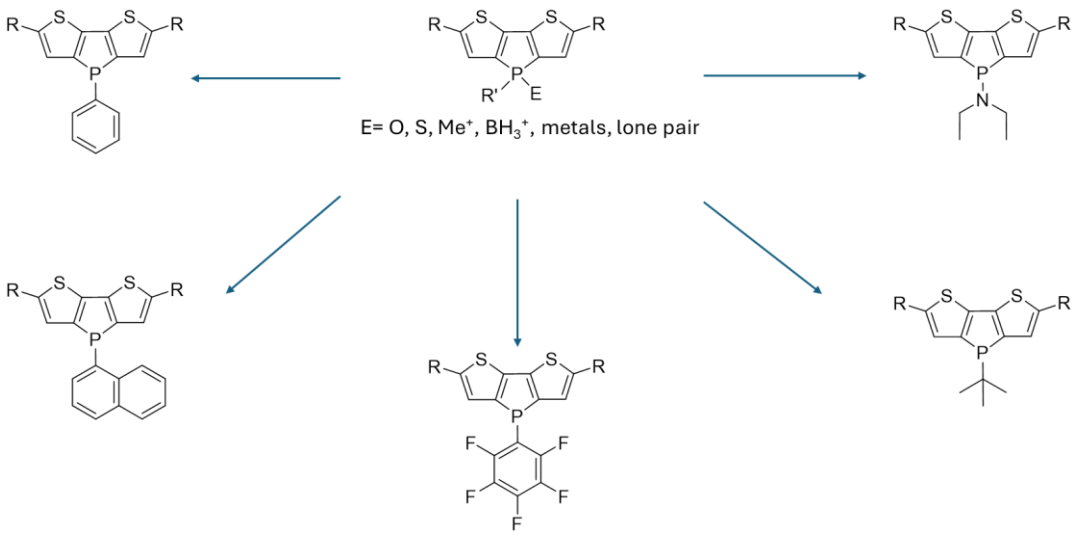

Figure 1-11: The dithienophosphole scaffold and various substituents on the phosphorus center.

Various substituents at the R' position (Figure 1-11) have been introduced during the ring-closure step of phosphole synthesis. The most used is the phenyl group, typically incorporated using dichlorophenylphosphane, resulting in highly stable phenyl-phosphole systems. Other substituents explored include tert-butyl, naphthyl, pyrenyl, amino, and pentafluorophenyl groups. These modifications result in the fine-tuning of the electronic structure and charge-transfer characteristics of the compounds. Additionally, the E position on the phosphorus center can be functionalized through straightforward reactions such as oxidation, sulfidation, or with borane (BH_3). At the R position, a variety of substituents such as phenyl, thienyl, naphthyl, and (diphenylamino)phenyl have been reported, each contributing to variations in emission properties and enabling control over the color output of these materials (Figure 1-12).[31–33]

The modification of the backbone in dithienophospholes opens up pathways for extending the conjugation of these materials, effectively reducing the band gap of the system. This adjustment allows for precise tuning of optical and electronic properties, shifting the emission wavelength throughout the visible spectrum. Consequently, backbone engineering emerges as one of the key design principles in developing various functional dithienophosphole materials. This structural modification is generally achieved by adding aryl substituents at the α-positions of dithienophosphole derivatives (Figure 1-12). In the Baumgartner group, such functionalization has been executed using established cross-coupling strategies, including Suzuki coupling, modified Suzuki–Miyaura protocols, and Stille-type reactions.[34]

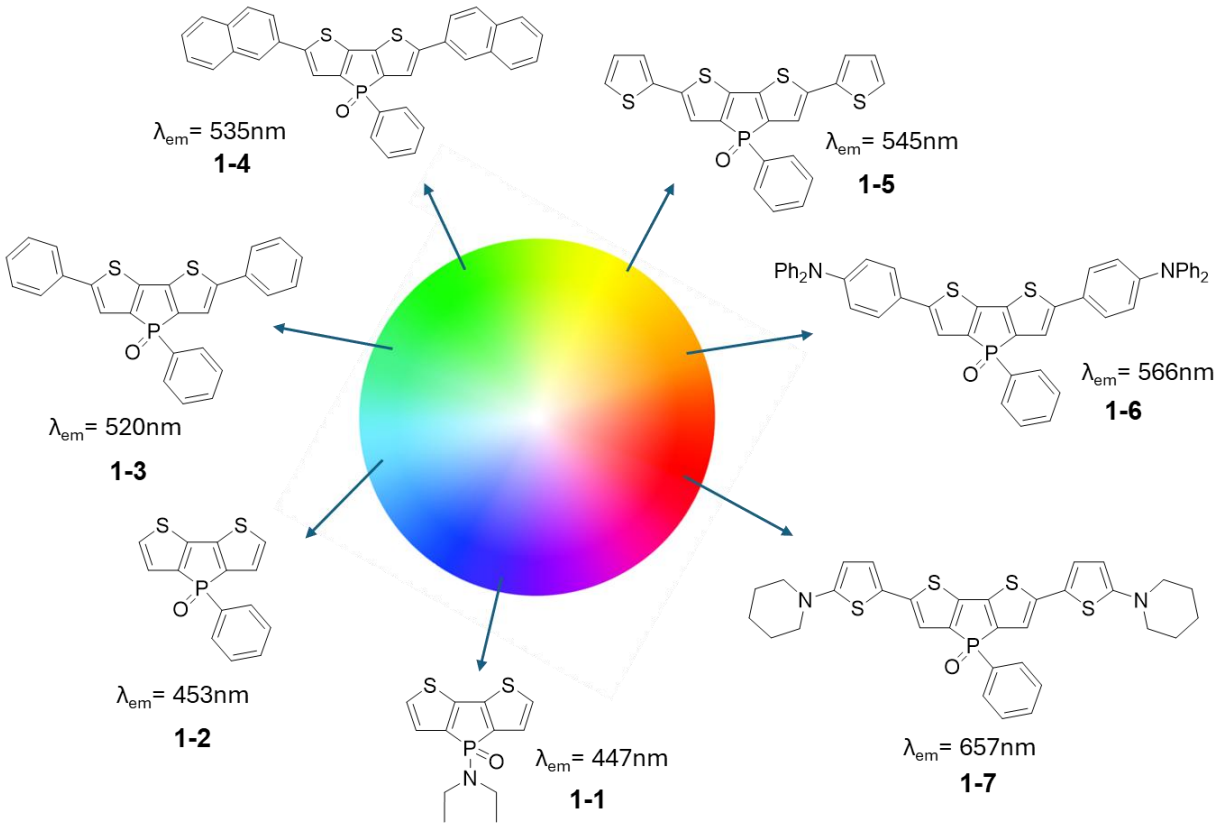

Figure 1-12: Varying emission colors from dithienophosphole derivatives.[34,35]

1.3.2 Self-Assembled Dithieno[3,2-*b*:2',3'-*d*]phosphole-based Materials

A) Phosphole lipids

In the pursuit of mimicking natural self-assembly to design functional organic π-conjugated materials, the Baumgartner group synthesized a series of dithienophosphole-based compounds whose organization is driven by π–π stacking, electrostatic interactions, and van der Waals forces. Among these, a notable class referred to as "phosphole lipids" demonstrated both mechano- and thermo-responsive behaviors. These molecules feature an ionic phosphorus center with a counterion, forming a polar head group, while long alkyl chains on the benzyl substituents create hydrophobic tails, structurally analogous to phospholipids in biological membranes (Figure 1-13A). This design facilitates the self-assembly of π-conjugated organophosphorus compounds into functional architectures.[36]

Phosphole lipids exhibit strong fluorescence, primarily due to the photophysics of the head group. Remarkably, these compounds also display aggregation-induced enhanced emission (AIEE), a phenomenon not typically observed in structurally related analogues (Figure 1-13B), indicating that molecular packing via self-assembly significantly enhances their photophysical properties. Additionally, compound **1-8** undergoes a visible color change in response to mechanical stimuli, which is attributed to conformational changes involving the rotation of the benzyl group. A mixture of compounds **1-8** (donor) and **1-9** (acceptor) further exhibits a mechanochromic response with the emission color shifting from blue to orange upon mechanical stress, highlighting their potential in stimuli-responsive optoelectronic applications.[36]

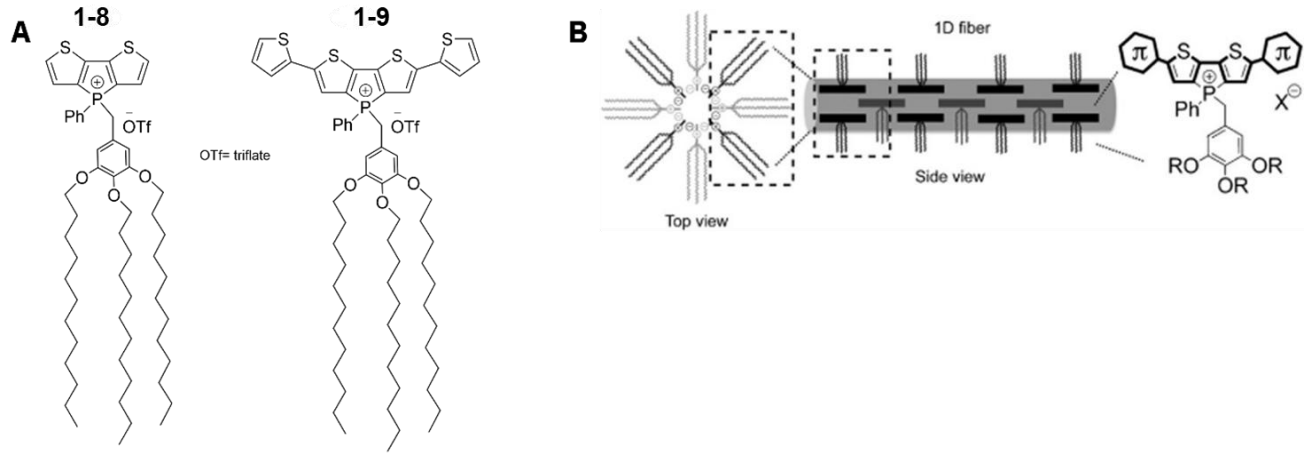

Figure 1-13: phosphole lipids. A) two phosphole lipids with distinct backbone, serving as a donor and acceptor for stimuli-sensitive tests. B) Probable molecular arrangement of phosphole lipids into 1D fiber (© John Wiley and Sons).[36]

B) Dithienophosphole-based Phosphinamides

The most recent work on dithienophosphole-based self-assembling materials focused on phosphinamides and the integration of hydrogen bonding for self-assembly, and alternating the substituents on the amide, to create mesogenic species; organogels and LCs (Figure 1-14). Compounds **1-11** and **1-12** have noteworthy packing compared to other self-assembled phospholes, as they pack head-to-head alignment instead of the typical head-to-tail packing driven by the polarity of the scaffold. These self-assembled phosphinamides also have dihedral angles between the NH and PO units ranging from 17° to 131°, owing to the rotational flexibility of the bonding along the P-N bond. It is important to note that the hydrogen bonding in CONH systems shows dihedral angle of either 0° or 180°. Hence, the hydrogen bonding involving a phosphorus center creates

additional flexibility that can accommodate more intermolecular assemblies. Due to the hydrogen bonding and the resulting orientation of the headgroups, the self-assembled dithienophosphole-based phosphinamides show hypsochromic photophysics, compared to their monomers. Hence, the hydrogen bonding increases the alignment of the conjugated scaffold to enhance the photophysical properties of these systems. Additionally, compound **1-13** successfully formed an organogel in hexanes, which was readily disrupted upon the introduction of a small amount of methanol. This reversible dissolution highlights the organogel's sensitivity to chemical stimuli.[31]

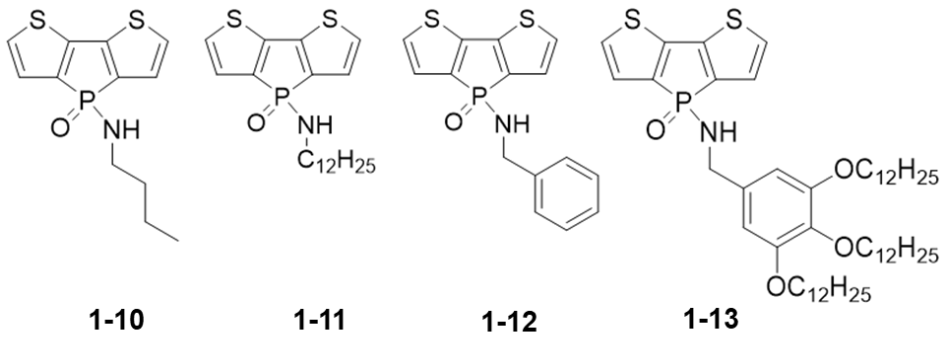

Figure 1-14: Structures of previous dithienophosphole-based phosphinamides

1.4 Scope of Thesis

As previously discussed, the growing field of organic π-conjugated materials continues to be an attractive route toward the development of next-generation sustainable energy and optoelectronic technologies. Among the materials investigated in our group, dithienophosphole-based phosphinamides have emerged as particularly promising due to their unique structural and functional attributes. The ability of these phosphinamides to

engage in hydrogen bonding contributes to enhanced intermolecular interactions, promoting better alignment and communication between chromophores in the solid state. This interaction introduces flexibility in the packing arrangements and is a key feature in enabling self-assembly into functional supramolecular architectures. Photophysically, the compounds demonstrate high photoluminescence quantum yield (PLQY) and exhibit hypsochromic shifts from solution to solid-state. These properties suggest efficient exciton confinement and radiative decay, which are desirable for emissive applications such as OLEDs. The dissolution of the organogel formed by one of the compounds confirms the system's sensitivity to external chemical stimuli and highlights its potential utility in responsive or sensory materials.

Motivated by these intriguing characteristics, this thesis focuses on extending the π-conjugation of these scaffolds through strategic backbone modifications. This molecular engineering aims to lower the HOMO-LUMO gap and enable precise tuning of emission wavelengths across the visible spectrum. Previous work has primarily focused on the development of blue emitters. Building upon that foundation, this project aims to synthesize green and orange emitters to enable the creation of materials with tailored optical properties suitable for application in WOLEDs. Following the blueprint established in the earlier study, the first objective is the synthesis of the green and orange emissive compounds. The second objective involves the substitution of the phosphorus center with benzylamine to generate model systems for investigating their self-assembly behavior. Their behavior, driven by rational design and molecular self-assembly, could offer a compelling approach for creating next-generation organic materials that bridge the gap between performance, responsiveness, and sustainability. Steps towards backbone

modifications and photophysical properties of resulting compounds will be discussed in Chapter 2. Chapter 3 will encompass substitution on the phosphorus center and studies of chromophore alignment and communication through Fluorescence Resonance Energy Transfer (FRET). Lastly, Chapter 4 will discuss conclusions and future work.

Chapter Two: π-Extended Dithienophosphole-based Phosphinamide Systems

2.1 Introduction

Organic π-conjugated materials have demonstrated significant potential across a wide range of applications, including electronics, photonics, energy conversion, and imaging. One of their key advantages lies in the tunability of their properties through the extension of π-conjugation, which allows for precise control over their optical and electronic behavior.[1,37] As discussed in the previous chapter, the degree of conjugation and the overall chemical structure play a crucial role in determining the optical, electronic characteristics, and the assembly behavior of these systems. The dithienophoshole system has been extensively investigated in our group with respect to its conjugation-dependent properties, as detailed in Section 1.3.1. Building upon this foundation, the present thesis continues to explore the strategic modification of conjugated frameworks as a means of tuning emission wavelengths for dithienophosphole-based phosphinamide systems. As the blue emitter has already been synthesized, this chapter focuses on the synthesis and characterization of the green and orange emitters.

2.2 Results and Discussion

2.2.1 Synthesis

Compound **1-1** was synthesized using the pre-established procedure.[33] The initial modification of the backbone involves preparing the precursor for subsequent Suzuki and Miyaura-type coupling reactions. This precursor is synthesized by brominating

dithienophosphole **1-1** using N-bromosuccinimide (NBS) in a 2:1 mixture of chloroform and acetic acid (Scheme 2-1). The successful formation of compound **2-1** is confirmed by NMR spectroscopy (^{1}H, $^{31}P\{^{1}H\}$, and $^{13}C\{^{1}H\}$), photophysical measurements and its structure in the solid state, obtained via single crystal X-ray crystallography. The crystals were grown from a mixture of toluene and hexanes. Due to the quality and nature of the crystals obtained, no further structural analysis can be reliably conducted. However, the crystal structure will be used solely to confirm the connectivity of compound **2-1**.

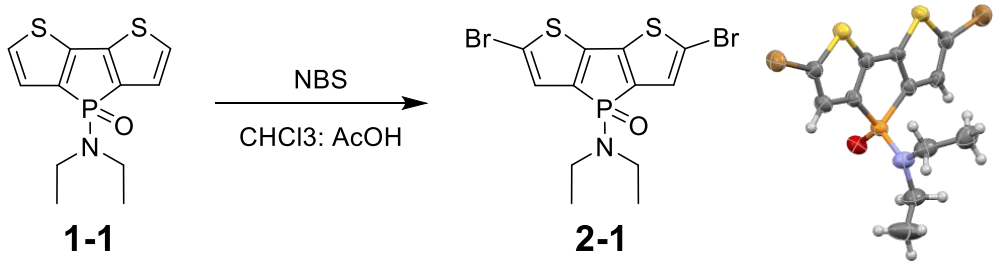

1-1 **2-1**

Scheme 2-1: Bromination of dithienophosphole for subsequent Suzuki coupling reactions.

Following the formation of the precursor, the target compounds were synthesized via a Suzuki coupling reaction for the green-emitting compound **2-2** and a Miyaura-type Suzuki coupling reaction for the orange-emitting compound **2-3**, respectively (Scheme 2-2). Their syntheses were carried out using different types of Suzuki coupling reactions, depending on the nature of the boron reagents involved. Traditional Suzuki coupling typically employs boronic acids, which are widely used due to their high reactivity and commercial availability. In contrast, Suzuki–Miyaura-type coupling utilizes boronic pinacol esters, which offer greater stability, ease of handling, and improved tolerance to air and moisture. The choice of coupling method was therefore guided by the specific boron-containing reagent available for each substrate.[38] The synthesis of **2-2** was carried out by refluxing

phenylboronic acid, tetrakis(triphenylphosphine)palladium(0), and potassium carbonate in a toluene–water mixture under an argon atmosphere for 16 hours. Following purification, a yellow solid was obtained in 39% yield. The synthesis of **2-3** was carried out by refluxing 4-dimethylborolanphenylamine, tetrakis(triphenylphosphine)palladium(0), and potassium carbonate in a tetrahydrofuran–water mixture under an argon atmosphere for overnight. Following purification, a burgundy solid was obtained in 85% yield. Their identities were confirmed by $^{31}P\{^{1}H\}$ NMR resonances at δ = 23.1 ppm and δ = 24.1 ppm, respectively. Their identities were further characterized by NMR spectroscopy (^{1}H, and $^{13}C\{^{1}H\}$), mass spectrometry, and photophysical measurements. Detailed synthetic procedures are provided in Section 2.4.

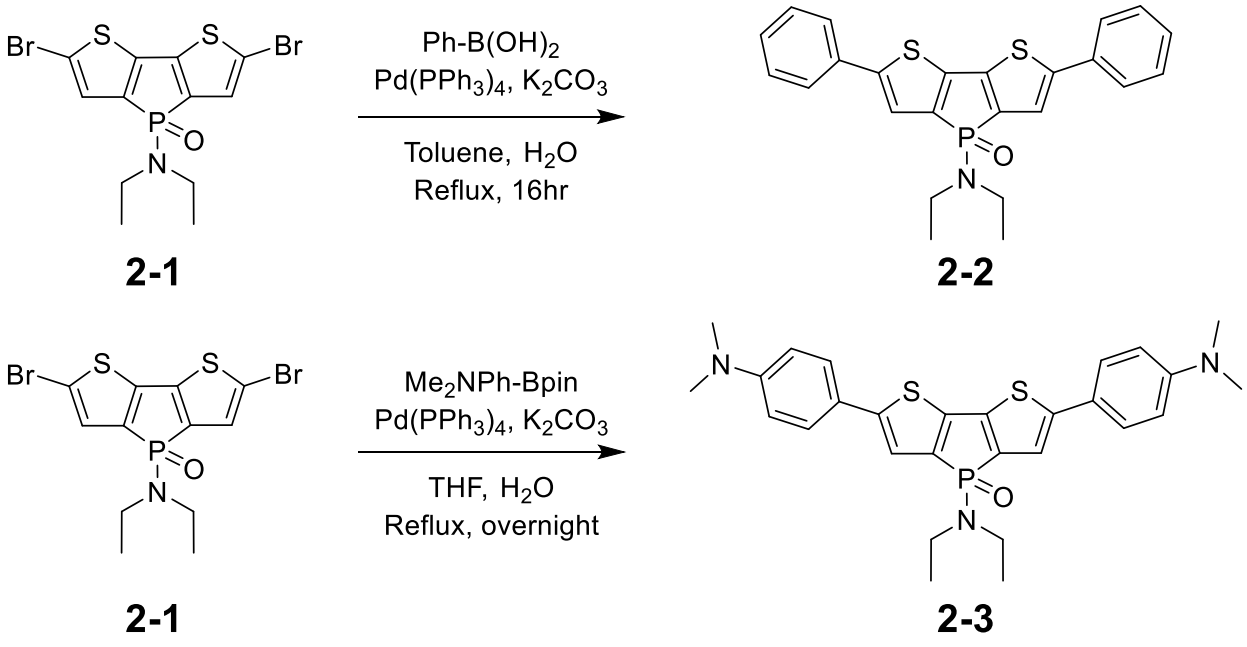

Scheme 2-2: Synthesis of green and orange dithienophosphole-based phosphinamide emitters via Suzuki coupling reactions.

2.2.2 Optical Properties

The optical properties of the newly synthesized emitters are thoroughly evaluated to gain deeper insight into their electronic structure and behavior. By examining parameters such as absorption spectra, emission characteristics, and quantum yields, a more comprehensive understanding of how molecular design influences their photophysical performance can be achieved. All spectra were obtained in DCM, $1x10^{-5}$ M (Figures 2-1 and 2-2). Compound **2-1** exhibits a single absorption peak at 382 nm, whereas compounds **2-2** and **2-3** each display two distinct absorption peaks in their UV-Vis spectra, (λ= 300 nm, 419 nm) and (λ= 332 nm, 470 nm), respectively (Table 2-1). In contrast, the emission spectra of all three compounds reveal a single emission peak. The phenylphosphole analogues of these compounds exhibit similar absorption and emission profiles. The analogue of compound **2-1** displays a single absorption peak, whereas the analogues of **2-2** and **2-3** show multiple absorption peaks with one corresponding emission peak.[34] The observation of two distinct absorption peaks for **2-2** and **2-3** suggests the presence of two distinct absorption transition moments, $S_0 \rightarrow S_1$ and $S_0 \rightarrow S_2$, likely arising from the extended π-conjugation in the molecules. Excitation of **2-2** and **2-3** at its two absorption wavelengths produced identical emission profiles. Similarly, excitation of **2-3** at its two absorption wavelengths produced identical emission profiles (Figure 2-1).

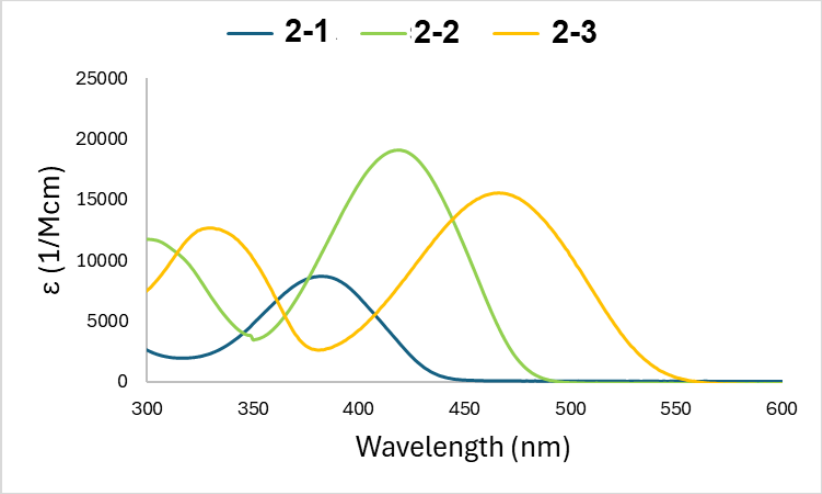

Figure 2-1: Absorption spectra of brominated and π-extended dithienophosphole-based phosphinamide systems (CH_2Cl_2; $1x10^{-5}$ M).

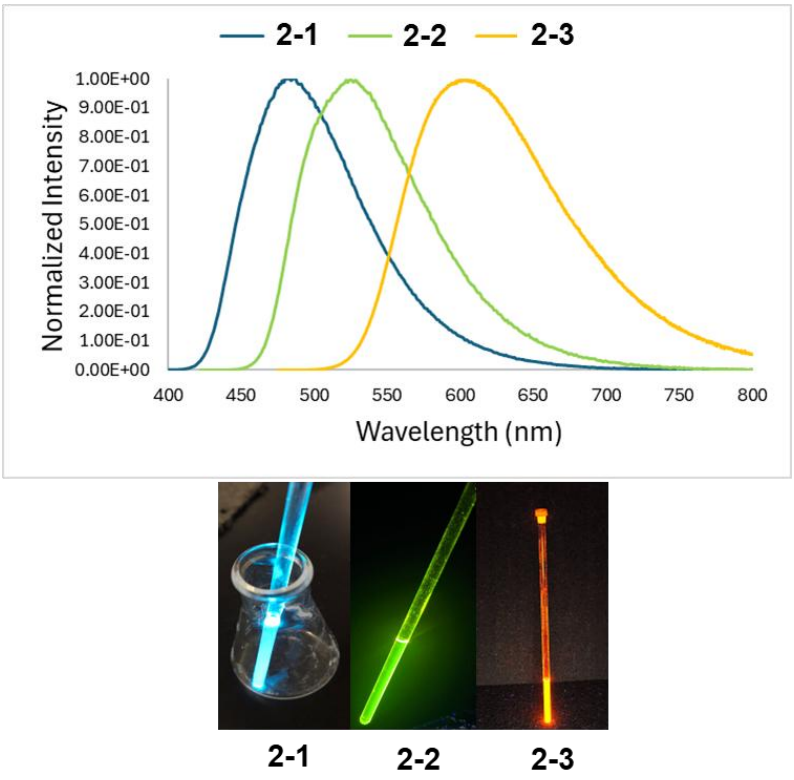

Figure 2-2: Emission spectra and colors of the brominated and π-extended dithienophosphole-based phosphinamide systems (CH_2Cl_2; $1x10^{-5}$ M).

The excitation spectra of **2-2** and **2-3** dictate their higher absorbance as the ideal wavelength for excitation. In contrast, compound **2-1** does not exhibit this dual excitation behavior, which can be attributed to the presence of a bromine atom at the α-position. This is also true for **1-10**, **1-11**, **1-12**, and **1-13** with a proton at the α-position of their phosphole moiety. Compound **2-1** emits in the blue region, compound **2-2** in the green, and compound **2-3** in the orange region of the visible spectrum (Figure 2-2).

Table 2-1: Absorption and Emission wavelengths (λ), extinction coefficients (ε), Stokes shifts, and PLQY of **2-1**, **2-2**, and **2-3** measured in CH_2Cl_2; $1x10^{-5}$ M.

Compound	λ_{Abs} (nm)	λ_{em} (nm)	ε ($M^{-1}cm^{-1}$)	Stokes Shift (cm^{-1})	PLQY (%)
2-1	382	485	8,700	5560	-
2-2	300 419	525	11,700 19,100	4820	-
2-3	332 470	602	12,700 15,500	4670	84.4

The extinction coefficients (ε) reported in Table 2-1 show a general increase for compounds **2-2** and **2-3** compared to compound **2-1**, indicating enhanced light absorption efficiency. This improvement is attributed to the extended π-conjugation present in

compounds **2-2** and **2-3**. Notably, compound **2-3** exhibits a higher extinction coefficient for the $S_0 \rightarrow S_2$ transition than compound **2-2**, which can be attributed to the strong electron-donating effect of its dimethylamine substituent. This group enhances the transition dipole moment, thereby increasing absorption at higher energy levels. In contrast, compound **2-2** displays a higher extinction coefficient for the $S_0 \rightarrow S_1$ transition compared to compound **2-3**. This difference is likely due to the increased planarity of compound **2-2**, which promotes better π-orbital overlap and more effective conjugation along the molecular backbone. In solution, the dimethylamine group in compound **2-3** may undergo rotational motion, reducing the overall planarity of the molecule and thus limiting the efficiency of the lower-energy $S_0 \rightarrow S_1$ transition.

Additional optical properties investigated include the Stokes shift and photoluminescence quantum yield (PLQY). A progressive decrease in the Stokes shift is observed from compound **2-1** (5560 cm^{-1}), **2-2** (4820 cm^{-1}) to compound **2-3** (4670 cm^{-1})**.** This trend is indicative of greater electronic and structural reorganization between the ground and excited states as the molecular frameworks become more conjugated and functionally complex. Notably, the pronounced Stokes shift observed in compound **2-1** is likely a result of enhanced intramolecular charge transfer (ICT) in the excited state, facilitated by the strong electron-donating diethylamine substituent. This interpretation is further supported by comparisons with previously synthesized analogs of compounds **2-1** and **2-2**, in which the phosphorus center bears a phenyl substituent instead of a diethylamine group. These analogs exhibited significantly smaller Stokes shifts, 4050 cm^{-1} for the analog of compound **2-1** and 2500 cm^{-1} for that of compound **2-2**.[34] This highlights the impact of electron-donating groups on excited-state behavior. A larger Stokes shift is generally

advantageous in optoelectronic applications, as it reduces reabsorption losses and enhances the color purity of the emission. Among the three compounds, only the PLQY of compound **2-3** was successfully measured. The PLQY values for compounds **2-1** and **2-2** could not be determined due to instrumental contamination and the limited availability of compound **2-2**, which had been fully consumed in subsequent synthetic steps, prior to measurements.

2.2.3 Density Functional Theory (DFT) Calculations

To better understand the electronic and optical properties of the compounds discussed in this chapter, DFT calculations were performed. The HOMO and LUMO energy levels, as well as the corresponding HOMO–LUMO energy gaps, were determined. In addition, the electron density distributions of these molecular orbitals were visualized to gain further insight into their electronic structures. All calculations were carried out using Gaussian at the Digital Research Alliance of Canada. Harmonic vibrational frequency analyses and geometry optimizations were performed for the molecular orbitals of 2-1, 2-2, and 2-3 at the B3LYP/6-31+G(d) level of theory in the gas phase. The HOMO and LUMO orbitals were to a mixed configuration, and calculations were performed using a total charge of 0 and a singlet spin multiplicity (multiplicity = 1). A consistent trend is observed in the spatial distribution of the frontier molecular orbitals across the series of compounds. The HOMO is primarily localized along the π-conjugated backbone, with minimal contribution from the sulfur and phosphorus atoms. In contrast, the LUMO is predominantly localized at the phosphole core and the sulfur atoms. This separation of orbital localization contributes to

the observed variation in the HOMO–LUMO energy gaps, which progressively decrease from compound **2-1** to compound **2-3**. This trend correlates well with the photophysical properties discussed earlier, particularly the red-shift in absorption and emission wavelengths associated with increased conjugation and enhanced charge-transfer character.

Table 2-2: The energy levels of the HOMO, LUMO, and the corresponding HOMO–LUMO energy gap for **2-1**, **2-2**, and **2-3**.

Compound	HOMO (eV)	LUMO (eV)	Δ_{H-L} (eV)
2-1	-5.98	-2.44	3.54
2-2	-5.49	-2.31	3.18
2-3	-4.78	-1.88	2.90

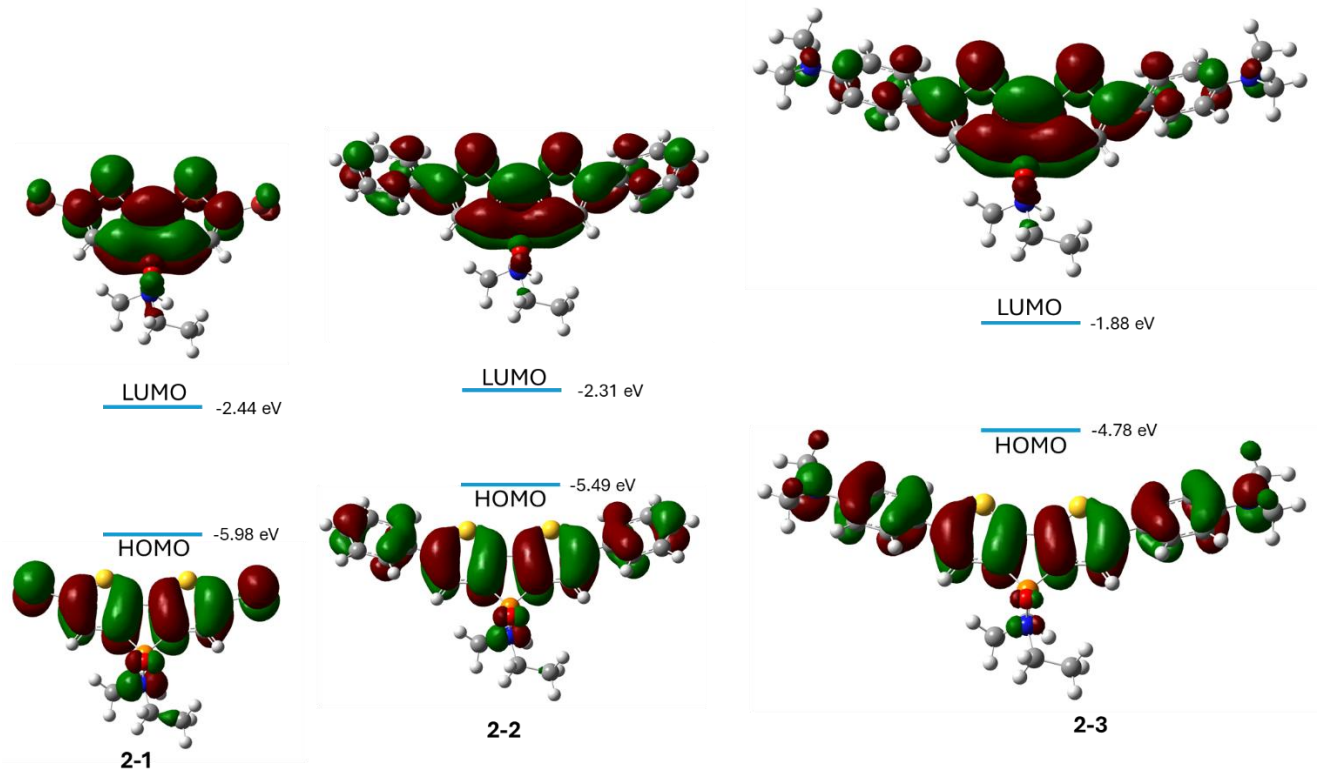

Figure 2-3: Molecular orbitals of **2-1**, **2-2**, and **2-3** with their energy levels (B3LYP/6-31+G(d) level of theory).

2.3 Conclusion and Outlook

In summary, this chapter has demonstrated the successful synthesis of compound **2-1** and its subsequent use in Suzuki coupling reactions to access green and orange-emitting compounds through extended π-conjugation. Compound **2-2** was synthesized via Suzuki coupling, while compound **2-3** was prepared using a Miyaura-type Suzuki coupling strategy. Photophysical analysis revealed a single excitation transition for the brominated precursor, whereas the π-extended systems exhibited two distinct excitation transitions, indicative of their enhanced conjugation. The observed Stokes shifts showed a clear linear trend and were significantly larger than those of their previously reported analogs,

highlighting the influence of the diethylamino substituent at the phosphorus center. While the extinction coefficients exhibited some variation, these discrepancies were attributed to the electron-donating nature and rotational flexibility of the dimethylamine substituent. Overall, the synthesized compounds displayed the targeted emission colors. The next chapter of this work will involve functionalization of the phosphorus center with benzylamine to produce model compounds for investigating the self-assembly behavior of these new emitters.

2.4 Experimental Section

2.4.1 General Considerations

Compound **1-1** was synthesized using pre-established procedure.[33] The synthesis of compound **2-1** was conducted under ambient conditions, while all other reactions were carried out under an argon atmosphere using standard Schlenk techniques. All commercially available reagents were used without further purification. Reaction progress was monitored by thin-layer chromatography (TLC) and by $^{31}P\{^{1}H\}$ NMR spectroscopy. Reagents were sourced from Sigma-Aldrich, Combi-Blocks, and Oakwood Chemical, and all solvents were obtained from Fisher Chemical. SPS-grade solvents (MBraun, Sigma-Aldrich) were used specifically in the synthesis of compounds **2-2** and **2-3**. NMR spectra (^{1}H, $^{31}P\{^{1}H\}$, and $^{13}C\{^{1}H\}$) were recorded using Bruker 400 MHz and 300 MHz NMR spectrometers equipped with a 5 mm ATM probe and operated with TOPSPIN software version 4.0.8. Chemical shifts are reported in parts per million (ppm), and multiplicities are denoted as follows: singlet (s), doublet (d), doublet of doublets (dd), triplet (t), quartet

(q), multiplet (m), and broad (br). UV–Vis absorption spectra were recorded at room temperature using an Agilent Technologies Cary 5000 UV-Vis spectrometer with 10 mm quartz cuvettes. All solvents used for UV–Vis measurements were obtained from Sigma-Aldrich. Emission measurements were conducted on an Edinburgh FS5 spectrofluorometer under identical conditions using solvents from Sigma-Aldrich and 10 mm quartz cuvettes.

2.4.2 Synthetic Procedures

Synthesis of **2-1**

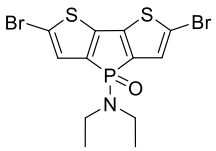

2-1

Compound **1-1** (0.43 g, 1.52 mmol) was dissolved in a mixture of acetic acid (30 mL) and chloroform (60 mL). N-Bromosuccinimide (1.08 g, 6.10 mmol) was added directly to the solution without prior dissolution, and the reaction mixture was stirred at room temperature for 3.5 hours. Upon completion, the reaction was quenched and neutralized using 0.5 M aqueous NaOH, followed by successive washes with water and brine. The organic layer was dried over anhydrous sodium sulfate and concentrated under reduced pressure. The resulting crude solid was washed with an acetone:chloroform mixture (14:1 v/v). The wash solvent was collected, passed through an alumina plug, and evaporated

to yield a pale solid (0.57 g, 85.2%). Crystallization from a toluene/hexane mixture afforded pure single crystals suitable for further analysis.

$^{31}P\{^{1}H\}$ NMR (162 MHz, $CDCl_3$): δ = 21.5 ppm.

^{1}H NMR (400 MHz, $CDCl_3$) δ = 7.05 (d, J = 2.7 Hz, 2H), 3.07 (dq, J = 12.3, 7.0 Hz, 4H), 1.08 (t, J = 7.1 Hz, 6H).

$^{13}C\{^{1}H\}$ (100 MHz, $CDCl_3$) δ = 144.3 (d, J = 27.3 Hz), 136.1 (d, J = 130.8 Hz), 127.9 (d, J = 13.9 Hz), 114.7 (d, J = 18.9 Hz), 38.4 (d, J = 5.4 Hz), 14.3 (d, J = 2.7 Hz).

Synthesis of **2-2**

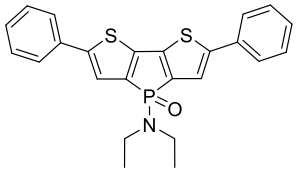

2-2

Phenylboronic acid (0.11 g, 0.89 mmol) and compound **2-1** (0.20 g, 0.44 mmol) were dissolved in toluene (50 mL). To this mixture, water was added followed by potassium carbonate (0.49 g, 3.54 mmol) and tetrakis(triphenylphosphine)palladium(0) [$Pd(PPh_3)_4$] (0.05 g, 0.04 mmol). The reaction mixture was then refluxed for 16 hours under an inert atmosphere. After completion, the reaction was cooled to room temperature and the mixture was extracted with toluene. The organic layer was dried over anhydrous sodium sulfate and filtered through a Celite plug. The crude product was subsequently washed with hexane, pentane, and diethyl ether to afford the purified compound (0.08 g, 39.3%).

$^{31}P\{^{1}H\}$ NMR (162 MHz, $CDCl_3$): δ = 23.1 ppm.

^{1}H NMR (400 MHz, $CDCl_3$) δ = 7.61 – 7.54 (m, 2H), 7.41 (t, J = 7.6 Hz, 2H), 7.35 – 7.28 (m, 2H), 3.16 (dq, 2H), 1.12 (t, J = 7.1 Hz, 3H).

$^{13}C\{^{1}H\}$ (100 MHz, $CDCl_3$) δ = 147.9 (d, J = 15.0 Hz), 143.6 (d, J = 27.5 Hz), 137.8 (d, J = 131.9 Hz), 133.6 (s), 129.2 (s), 128.2 (s), 125.7 (s), 121.0 (d, J = 14.0 Hz), 38.6 (d, J = 5.4 Hz), 14.4 (d, J = 2.8 Hz).

Synthesis of **2-3**

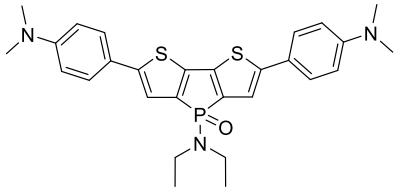

2-3

Compound **2-1** (0.03 g, 0.06 mmol), dimethylborolanphenylamine (0.03 g, 0.12 mmol), and potassium carbonate (0.05 g, 0.37 mmol), were added to a Schlenk flask and subjected to evacuation under vacuum. Tetrahydrofuran (THF) was then introduced into the flask, followed by the addition of $[Pd(PPh_3)_4]$ (0.004g, 0.004 mmol). Subsequently, water (5 mL) was added to initiate the reaction. The mixture was refluxed under an inert atmosphere, and upon completion, allowed to cool to room temperature. Chloroform was then added to the mixture, and the solution was filtered through a Celite plug. The filtrate was dried over anhydrous sodium sulfate and concentrated under reduced pressure using a rotary evaporator. The resulting solid was washed sequentially with diethyl ether and hexanes to afford the final red solid (0.03 g, 85%).

$^{31}P\{^{1}H\}$ NMR (162 MHz, $CDCl_3$): δ = 24.1 ppm.

^{1}H NMR (400 MHz, $CDCl_3$) δ = 7.47 – 7.39 (m, 2H), 7.10 (d, *J* = 3.0 Hz, 1H), 6.76 – 6.68 (m, 2H), 3.14 (dq, *J* = 12.1, 7.1 Hz, 2H), 3.00 (s, 5H), 1.10 (t, *J* = 7.1 Hz, 3H).

^{13}C NMR (101 MHz, $CDCl_3$) δ = 150.3 (s), 148.4 (d, *J* = 30.3 Hz), 142.0 (d, *J* = 27.8 Hz), 137.5 (s), 136.2 (s), 126.7 (s), 122.0 (s), 118.6 (d, *J* = 14.1 Hz), 112.5 (s), 77.2 (s), 40.4 (s), 38.5 (d, *J* = 5.4 Hz), 14.4 (d, *J* = 2.7 Hz).

Theoretical mass: 521.1724 g/mol HRAM MS m/z 522.1785 g/mol

Chapter Three: Synthesis of Self-Assembly Model Compounds

3.1 Introduction

This Chapter focuses on the substitution of benzylamine at the phosphorus center to access compounds that constitute model compounds for the ultimate target species that promote self-assembly via hydrogen bonding. In this context, the development of two model compounds with green and orange emission was targeted. The substitution was successfully achieved for the green emitter; however, similar modification strategies proved to be challenging for the orange emitter. These synthetic difficulties are explored in detail within this chapter. As a remediation strategy, alternative emitters incorporating different electron-donating substituents were targeted. Specifically, 2-thienyl and 4-methoxyphenyl derivatives were synthesized via cross-coupling reactions, following similar methodologies outlined in Chapter 2. The subsequent benzylamine substitution at the phosphorus center of these new systems is also discussed. Finally, Förster Resonance Energy Transfer (FRET) studies between the previously reported blue model emitter **1-12** and the new green emitter bearing a benzylamine substituent are presented to investigate their potential for energy transfer and potential supramolecular organization.

3.2 Results and Discussion

3.2.1 Synthesis

The synthesis of compound **3-2** follows a previously reported procedure used for preparing the blue emitter **1-12** featuring benzylamine at the phosphorus center.[31] The

process begins with the treatment of the phosphole precursor **2-2** using 1 N HCl, during which the solid is suspended in the acidic solution. The acid is subsequently removed by thorough washing with water, yielding the intermediate **3-1**. Under an inert atmosphere, this intermediate is then reacted with thionyl chloride ($SOCl_2$) in the presence of catalytic amounts of dimethylformamide (DMF) to activate the phosphorus center by producing a chlorophosphole oxide. This is followed by the addition of benzylamine, resulting in the formation of the target compound, obtained in a yield of 56%. The compound was fully characterized by ^{1}H, $^{31}P\{^{1}H\}$, and $^{13}C\{^{1}H\}$ NMR spectroscopy, mass spectrometry, and optical spectroscopies. All attempts to grow single crystals were unsuccessful, thereby preventing further investigation of solid-state characteristics.

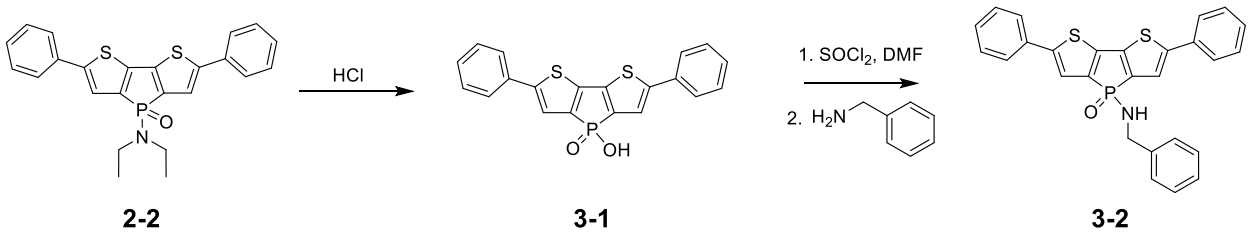

2-2 **3-1** **3-2**

Scheme 3-1: synthetic pathway for green model compound **3-2**.

The initial attempt to synthesize compound **3-4** followed the same procedure as described for compound **3-2** (Scheme 3-2A). However, during the first step, protonation of the dimethylamino group on the phenyl ring occurred, altering the solubility of the compound. Instead of remaining as a suspended red solid, as observed with the original compound, the material became fully soluble in water, appearing as a yellow solution. This protonation behavior has been previously observed in related studies in our group by Carlos Romero-Nieto and Huy Hyunh.[35,39] To recover the product, the solution was treated with a base to deprotonate the amine group and render the compound insoluble.

The resulting precipitate was then collected by filtration. However, most of the product adhered strongly to the filter paper, making it difficult to recover, and a significant portion was lost during this process.

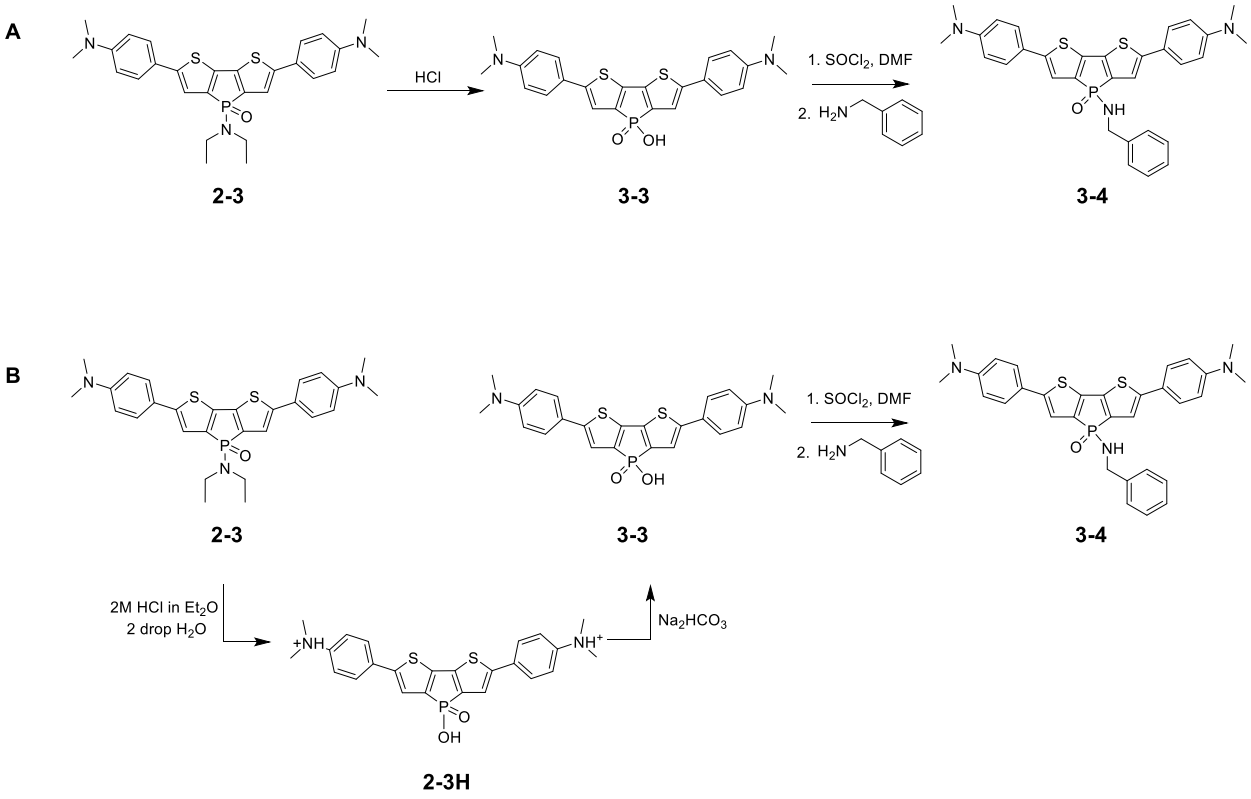

Scheme 3-2: Initial and final synthetic pathway for compound **3-4**.

Modifications to the synthetic procedure were undertaken in an effort to obtain the target compound. As these species represent the first examples of dithienophosphole-based phosphinamide systems, procedural adjustments were based on a trial-and-error approach. One such attempt involved eliminating water from the reaction entirely. The precursor was suspended in a 2 M HCl solution in dry diethyl ether and stirred overnight under inert atmosphere, with the aim of directly generating the corresponding chlorophosphole oxide intermediate, thereby bypassing the use of thionyl chloride and

DMF. The resulting product was a non-fluorescent grey solid. It was suspected that residual HCl in the reaction mixture may have inhibited the subsequent reaction with benzylamine, possibly by interfering with nucleophilic attack at the phosphorus center. In a subsequent attempt, the solid was thoroughly washed with fresh dry ether before reacting it with benzylamine, yet the outcome remained unchanged. I hypothesize that chlorination of the phosphole did not occur under these conditions, and that only the dimethylamine group on the phenyl ring was protonated. As a result, the intermediate failed to react with benzylamine, preventing formation of the desired product.

Given this observation, the presence of water might be essential for the formation of **3-4**, allowing the reaction to proceed via the originally established pathway. The earlier procedure was thus repeated, including the base treatment and filtration step. To recover as much product as possible, the filter paper was scraped and washed using chloroform, though some filter paper residue was inevitably carried over. This crude material was subjected to the subsequent reaction steps. The appearance of orange fluorescence at the end of the process indicated potential success, although multiple peaks were observed in the $^{31}P\{^{1}H\}$ NMR spectrum. Mass spectrometry analysis nonetheless confirmed the presence of the desired compound.

To avoid the filtration step while still retaining water in the initial reaction, the conditions were modified by adding 2 M HCl in diethyl ether to the starting material along with two drops of water. The mixture was stirred overnight, and the solid turned yellow, with minimal water present. This is an indication that **2-3H** was formed (Scheme 3-2B). After thorough washing with dry diethyl ether to remove residual acid, and drops of base, acetone was added to extract any remaining water. The solid was then dried directly in

the reaction flask. Transfer to a Schlenk flask for the subsequent thionyl chloride and DMF treatment was performed using chloroform with sonication. This approach also yielded an orange-fluorescent solution with three $^{31}P\{^{1}H\}$ NMR peaks (20.9, 20.3, 19.8 ppm). Mass spectrometry once again confirmed the formation of the targeted compound. However, purification attempts were ultimately unsuccessful. Specifically, washing the crude product with diethyl ether led to decomposition, and a new peak appeared at 10.1 ppm in the $^{31}P\{^{1}H\}$ NMR spectrum, indicating possible side-product formation or degradation.

Table 3-1: Procedure modifications for benzylamine substitution to synthesize **3-4**.

Rationale	Modification	Resulting observation
To remove the dissolved solid from water	Addition of base and gravity filtration	Adsorption to filter paper
No filtration necessary and simpler steps.	No water, $SOCl_2$, DMF	Grey solid that does not fluoresce
To remove solids from filter paper	Scrape and wash filter paper with chloroform	Orange emission with multiple $^{31}P\{^{1}H\}$ NMR peaks
Avoid filter paper use	Add a couple drops of water to initial reaction	Orange emission with three $^{31}P\{^{1}H\}$ NMR peaks

While efforts to synthesize compound **3-4** were still ongoing, alternative target compounds **3-5** and **3-6** to eliminate the encountered challenges were pursued (Scheme 3-3). Given the electron-accepting nature of the phosphole core, introducing electron-accepting groups along the conjugated π-backbone often counteracts red-shifting by

reducing the overall donor–acceptor push–pull character. As a result, the strategy focused on incorporating other electron-donating substituents to achieve red-shifted emission. Two terminal aryl substituents, 2-thienyl and 4-methoxyphenyl, were selected for this purpose. However, these groups are anticipated to induce only moderate red-shifting compared to the strongly electron-donating dimethylaniline substituent previously used. Among them, the 2-thienyl species is expected to produce yellow emission, as evidenced by a previously reported phosphole analogue bearing this group and a phenyl substituent at the phosphorus center, which emits at 545 nm.[34] The second substituent, 4-methoxyphenyl, is even less electron-donating than thiophene and is therefore not expected to achieve the same bathochromic shift observed with dimethylaniline. An additional advantage of these new substituents is their reduced tendency to protonate under acidic conditions, unlike the dimethylaniline group, which posed challenges during functionalization. Incorporating these emitters into a WOLED system would likely shift the color balance toward a cooler white tone, if combined with blue and green emitters, resulting in a yellow–green–blue blend instead of the initially intended orange–green–blue configuration.

Similar to the precursor species described in Chapter 2, these newly developed emitters were also synthesized by extending π-conjugation at the α-position of the dithienophosphole backbone. Specifically, compounds **3-5** and **3-6** were obtained through Suzuki and Miyaura-type Suzuki couplings using a common precursor, compound **2-1**. Compound **3-5** was synthesized via Suzuki coupling with methoxyphenylboronic acid and compound **2-1**, following the same general methodology employed in the synthesis of **2-2**. Likewise, compound **3-6** was prepared using a similar

approach to that used for synthesizing **2-3**. The Miyaura coupling reaction was carried out using thiophene-2-boronic acid pinacol ester and compound **2-1** to complete the formation of the target structure (Scheme 3-3). After workup and purification, 69% of **3-5** and 74% of **3-6** were obtained. These compounds were fully characterized by ^{1}H, $^{31}P\{^{1}H\}$, and $^{13}C\{^{1}H\}$ NMR spectroscopy, mass spectrometry, and optical spectroscopies.

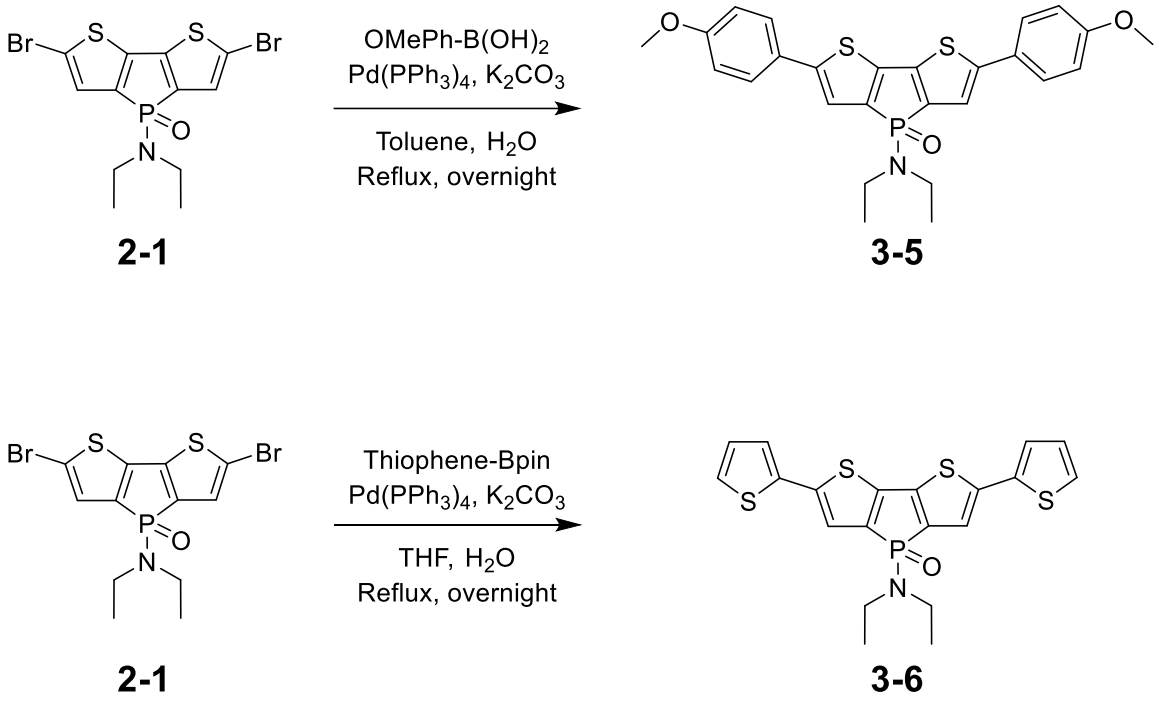

Scheme 3-3: Synthesis of yellow emitting dithienophosphole-based phosphinamide emitters via Suzuki coupling reactions.

The next step involved synthesizing model compounds for the newly π-extended emitters. Following the established methodology (Scheme 3-4), the starting materials **3-5** and **3-6** were suspended under acidic conditions in separate reaction flasks. Notably, both compounds remained suspended during this initial treatment. This was an encouraging sign, as it suggested that the protonation of the new thiophene and methoxy substituents

has been avoided. However, upon completing the subsequent steps, unexpected results emerged. Both products exhibited blue emission rather than the characteristic yellow emission observed in their parent compounds. When spotted on a TLC plate, neither compound showed any mobility, likely due to strong interactions with the polar silica or alumina surfaces. Further investigation revealed signs of decomposition and instability. Compound **3-8** fully decomposed during an attempted extraction with chlorobenzene, evidenced by the shift in its $^{31}P\{^{1}H\}$ NMR signal from 14.2 ppm to a mixture of peaks at 29.5 and 6.7 ppm. Efforts to purify compound **3-10** via diethyl ether wash yielded a species with a doublet at 15.4 ppm and an additional peak at 7.4 ppm in its $^{31}P\{^{1}H\}$ NMR spectrum. However, mass spectrometry analysis after this wash nonetheless confirmed the presence of **3-10**. Unfortunately, despite these efforts, further purification was unsuccessful. Since the thienyl and methoxyphenyl substituents in these compounds cannot easily be protonated, the observed instability and side reactions are most likely occurring at the phosphorus center. The exact mechanisms and pathways of these decompositions remain unclear and warrant further investigation for future works.

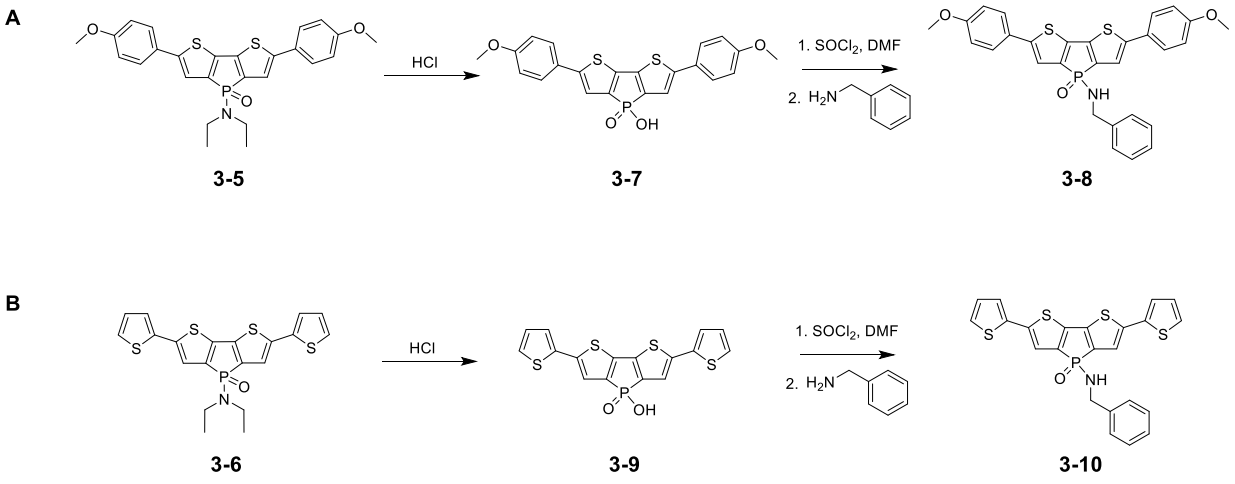

Scheme 3-4: Synthetic pathway for yellow model compounds **3-8** and **3-10**.

3.2.2 Optical Properties

Similar to the precursor species synthesized in Chapter Two, the optical properties of the species discussed in this Chapter are thoroughly evaluated to gain deeper insight into their electronic structure and behavior. By examining parameters such as absorption features, emission characteristics, and photoluminescence quantum yields (PLQYs), a more comprehensive understanding of how molecular design influences their photophysical performance can be achieved.

The absorption spectrum of the green model compound **3-2**, displays two distinct peaks, mirroring the behavior of its parent compound **2-2**. The higher-energy absorption peak appears at 320 nm, largely differing from the corresponding $S_0 \rightarrow S_2$ transition in the parent compound at 300 nm. Additionally, the lower-energy absorption, attributed to the $S_0 \rightarrow S_1$ transition, occurs at 419 nm in both the model compound and its precursor. Despite these similarities, their emission wavelengths differ by 8 nm, with the model compound emitting at 533 nm compared to 525 nm for the precursor compound. In terms of extinction coefficients, the two compounds show comparable values for the higher-energy absorption, 10,000 $M^{-1}cm^{-1}$ vs. 11,700 $M^{-1}cm^{-1}$, but the green model compound exhibits a significantly larger extinction coefficient for the lower-energy absorption, 25,300 $M^{-1}cm^{-1}$ vs. 19,100 $M^{-1}cm^{-1}$. This enhancement in light absorption efficiency at the lower-energy transition may be attributed to improved electronic coupling introduced by the substitution benzylamine at the phosphorus center, potentially enhancing transition probability. Likewise, their Stokes shifts differ by a noticeable margin. The model compound exhibits a larger Stokes shift of 5110 cm^{-1}, compared to 4820 cm^{-1} for the parent compound. This increase can be attributed to the enhanced structural relaxation

in the excited state and greater intramolecular charge transfer (ICT) behavior introduced by the benzylamine substitution. The presence of the benzylamine group likely increases conformational freedom and polarity changes between the ground and excited states, resulting in a greater energy difference between absorption and emission. Lastly, the PLQY of the green model compound is 95.6%, which is highly beneficial for application as emitter in OLED devices.

The photophysical properties of the red-shifted emitters **3-5** and **3-6** are reported in Table 3-2 below. The two compounds have two distinct absorption peaks, a trend that is consistent with the π-extended systems seen in this thesis. Their higher-energy absorption peaks are quite similar, occurring at 306 nm and 314 nm for compounds **3-5** and **3-6**, respectively. The lower-energy absorption transitions are observed at 427 nm and 438 nm for these same compounds. Interestingly, despite the noticeable difference in their absorption profiles, both compounds exhibit nearly identical emission maxima at 550 nm and 551 nm. This similarity in emission could be due to the fact that the substituents, methoxybenzene and thiophene, are not sufficiently electron-donating to induce significant ICT character or strong electronic perturbation in the excited state. As a result, their emission is governed more by the intrinsic properties of the phosphole than by the nature of the substituents. It may also suggest that upon excitation, both systems undergo similar relaxation pathways, converging to an emissive state that is energetically similar regardless of the substituent. This behavior highlights the dominant role of the core conjugated system in dictating the photophysical properties when substituents are only moderately donating. The two compounds show comparable values for higher-energy absorption, 11,100 $M^{-1}cm^{-1}$ vs. 10,500 $M^{-1}cm^{-1}$, but the **3-6** exhibits a significantly

larger extinction coefficient for the lower-energy absorption (20,600 $M^{-1}cm^{-1}$ vs. 12,300 $M^{-1}cm^{-1}$). On the contrary, **3-5** exhibits a larger Stokes shift of 5240 cm^{-1}, compared to **3-6**, with a Stokes shift of 4680 cm^{-1}. This difference may be attributed to the greater rotational flexibility of the methoxyphenyl substituent in **3-5**, which can lead to enhanced excited-state structural relaxation relative to the more rigid thiophene substituent in **3-6**. Lastly, the PLQY of **3-5**, 94.7%, is significantly higher than **3-6**, 57.4%.

Table 3-2: Absorption and Emission wavelengths (λ), extinction coefficients (ε), Stokes shifts, and PLQY of **3-2**, **3-5**, and **3-6** measured in CH_2Cl_2; $1x10^{-5}$ M.

Compound	λ_{Abs} (nm)	λ_{em} (nm)	ε ($M^{-1}cm^{-1}$)	Stokes Shift (cm^{-1})	PLQY (%)
3-2	320 419	533	10,000 25,300	5100	95.6
3-5	306 427	550	11,100 12,300	5240	94.7
3-6	314 438	551	10,500 20,600	4680	57.4

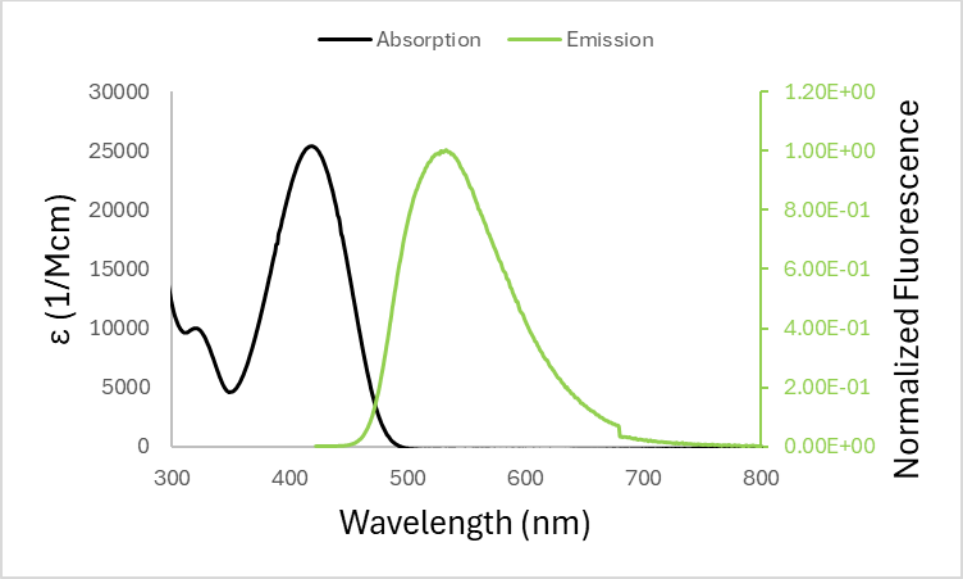

Figure 3-1: Absorption and emission spectra of **3-2** (CH_2Cl_2; $1x10^{-5}$ M).

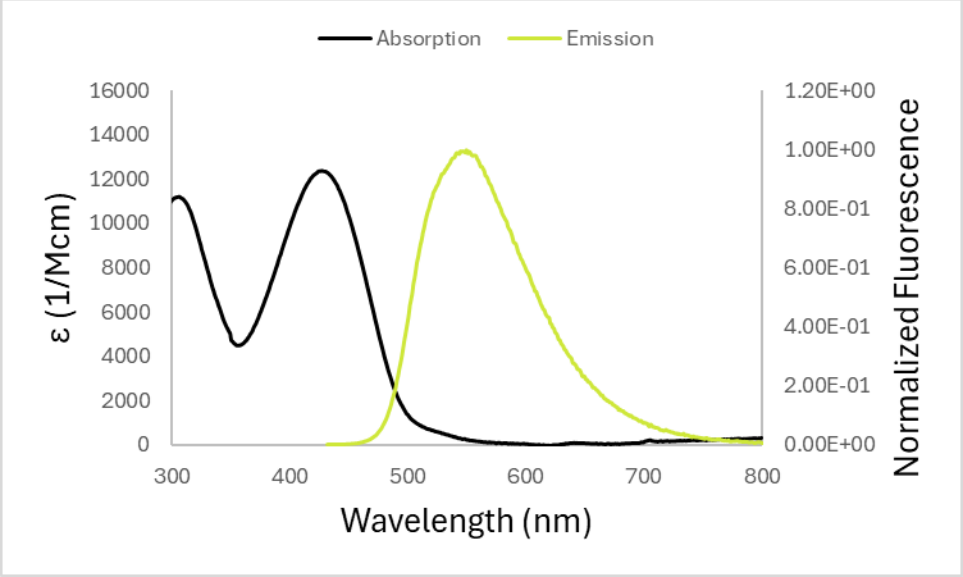

Figure 3-2: Absorption and emission spectra of **3-5** (CH_2Cl_2; $1x10^{-5}$ M).

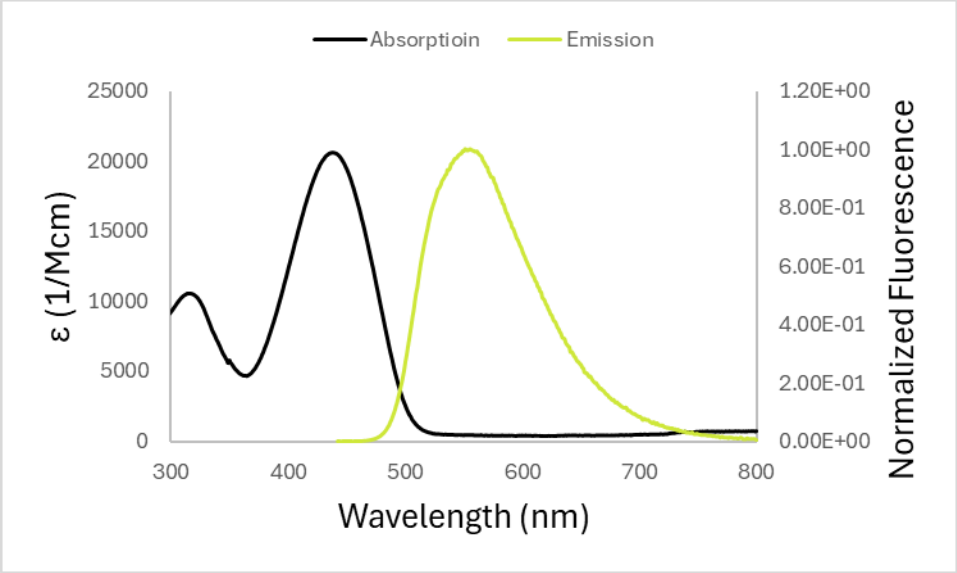

Figure 3-3: Absorption and emission spectra of **3-6** (CH_2Cl_2; $1x10^{-5}$ M).

3.2.3 Density Functional Theory (DFT) Calculations

To better understand the electronic and optical properties of the compounds discussed in this Chapter, DFT calculations were performed at the B3LYP/6-31+G(d) level of theory (Refer to page 32 for calculation setup). The LUMO, HOMO and Δ_{H-L} of the alternative, red-shifted emitters, **3-5** and **3-6**, are compared first, followed by those of all the model compounds.

The HOMO (-5.21 eV) and LUMO (-2.12 eV) energies of **3-5** are higher than the corresponding HOMO (-5.39 eV) and LUMO (-2.43 eV) energies of **3-6** (Figure 3-4). The HOMO-LUMO energy gap for compound **3-6** with 2.96 eV is slightly smaller compared to **3-5**, measuring 3.09 eV. This trend reflects the stronger electron-donating nature of the thiophene substituents compared to the methoxyphenyl group, which promotes ICT.

Similar to other dithienophospholes in this thesis, the HOMO levels of both compounds primarily reside on the conjugated backbone, with minimal contributions from sulfur and phosphorus atoms. Conversely, the LUMOs are mainly located on the sulfur and phosphole core. The model compound **3-2**, as expected, exhibits the highest HOMO–LUMO energy gap at 3.20 eV. The methoxyphenyl-substituted model, **3-8** follows with a second-largest gap of 3.11 eV and has the second highest-lying HOMO and LUMO levels. Compound **3-10** displays the second-lowest HOMO–LUMO gap at 3.02 eV, with both frontier orbitals situated lower in energy compared to **3-8**. These energies align with what is observed in their parent compounds **3-5** and **3-6**.

Table 3-3: The HOMO and LUMO energy levels and the corresponding HOMO–LUMO energy gaps for **3-2**, **3-4**, **3-5**, **3-6**, **3-8** and **3-10**.

Compound	HOMO (eV)	LUMO (eV)	$\Delta_{H\text{-}L}$ (eV)
3-2	-5.56	-2.36	3.20
3-4	-4.83	-1.93	2.90
3-5	-5.21	-2.12	3.09
3-6	-5.39	-2.43	2.95
3-8	-5.27	-2.16	3.11
3-10	-5.48	-2.46	3.02

Lastly, compound **3-4** shows the smallest HOMO–LUMO energy gap at 2.90 eV, and notably, its HOMO and LUMO are the highest in energy within the series. Overall, the

DFT-calculated trends in HOMO–LUMO gaps correlate well with the experimental absorption data.

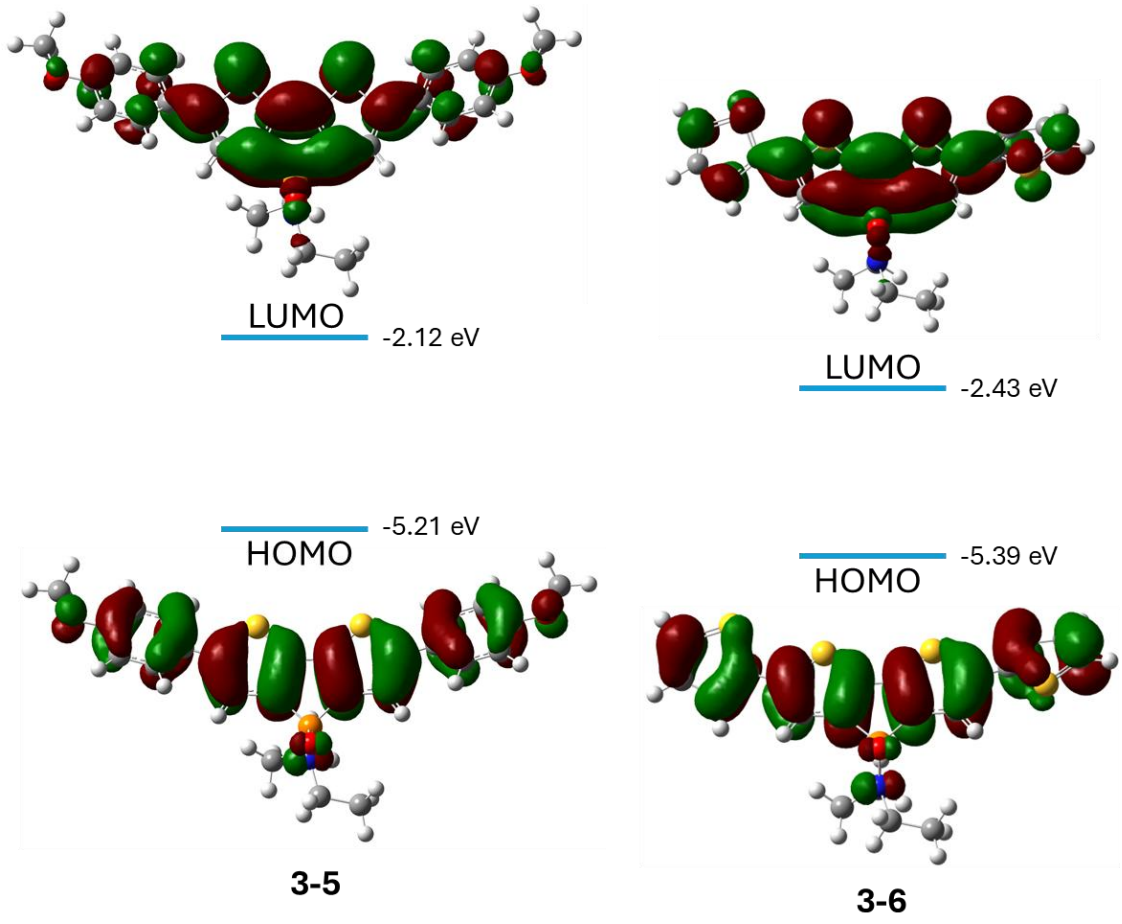

Figure 3-4: Molecular orbitals of compounds **3-5**, and **3-6**, the two new emitters, with their energy levels arranged in decreasing order of HOMO–LUMO gap energies (B3LYP/6-31+G(d) level of theory).

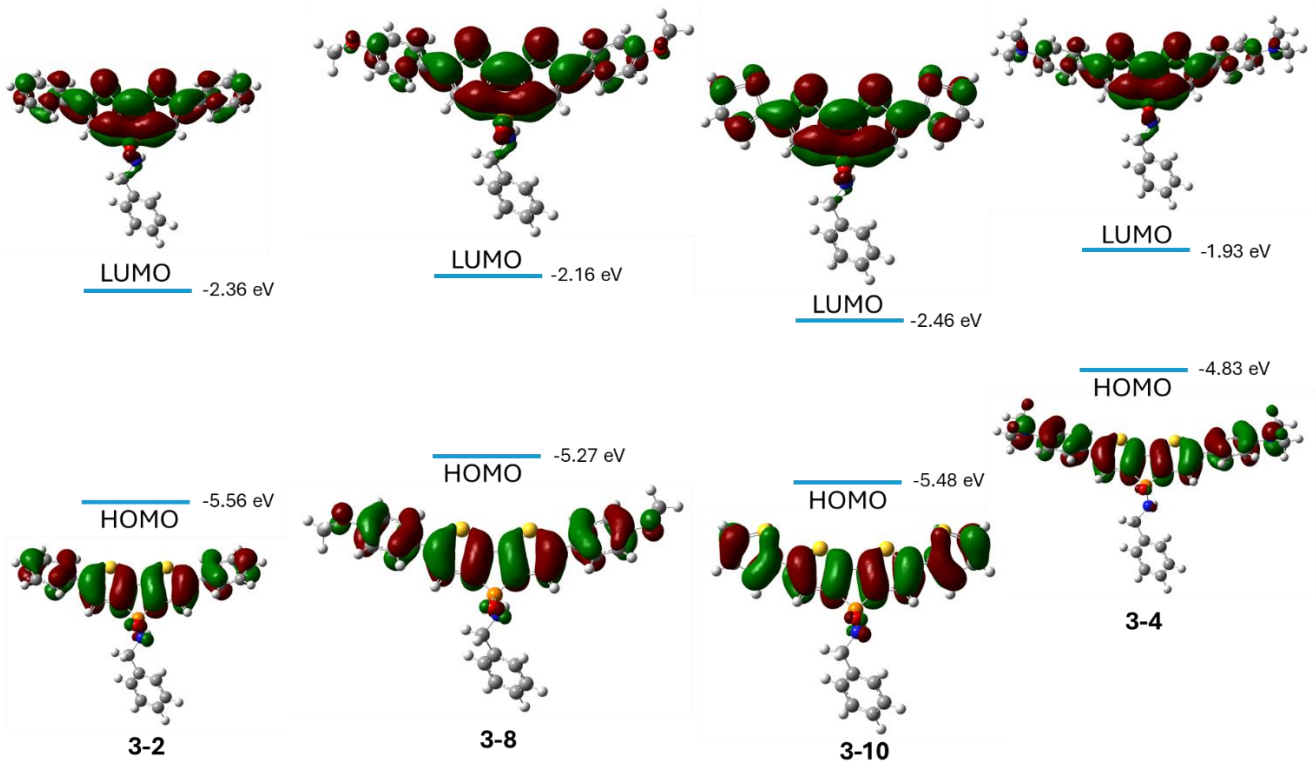

Figure 3-5: Molecular orbitals of compounds **3-2**, **3-4**, **3-8**, and **3-10**, the targeted model compounds, with their energy levels arranged in decreasing order of HOMO–LUMO gap energies (B3LYP/6-31+G(d) level of theory).

3.2.4 Förster Resonance Energy Transfer (FRET) Studies

Förster Resonance Energy Transfer (FRET) is a powerful spectroscopic technique used to measure nanoscale distances and investigate molecular interactions between a donor and an acceptor molecule. First theoretically described in 1948, FRET is effective over distances typically ranging from 1 to 10 nm. FRET proceeds via a nonradiative mechanism, which can be described by both classical Coulombic dipole–dipole interactions and quantum mechanical principles. The efficiency of energy transfer serves

as an indicator of the relative distance between the donor and acceptor, collectively referred to as the FRET pair. The efficiency of FRET depends on several critical factors, including the spectral overlap between the donor's emission spectrum and the acceptor's absorption spectrum, which directly influences the likelihood of energy transfer. In addition, the relative orientation of the transition dipole moments of the donor and acceptor plays a significant role; maximum efficiency is achieved when these dipoles are favorably aligned. Both of these factors, along with the distance between the donor and acceptor, collectively determine the overall efficiency of the energy-transfer process.[40]

Organic conjugated systems have garnered significant interest due to their promising optoelectronic properties, as discussed in Chapter One. Also emphasized in Chapter One is the strategic use of hydrogen bonding to facilitate the self-assembly of highly ordered structures. This approach enables modulation of chromophore spatial arrangement, which in turn can influence exciton migration pathways. Such control is beneficial for optimizing the performance of light-harvesting devices, sensors, and other optoelectronic applications such as WOLEDs. FRET has been widely employed to study supramolecular interactions in conjugated systems, providing insight into intermolecular distances, assembly behavior, and energy-transfer dynamics.[41,42] As part of this thesis, initial FRET between the blue (**1-12**) and green (**3-2**) model compounds capable of engaging in hydrogen bonding and other supramolecular interactions was investigated. By analyzing the spectral overlap between the donor's emission spectrum and the acceptor's absorption spectrum, and by measuring the energy transfer efficiency (E), the Förster radius (R_0) and the donor–acceptor separation distance (r) can be calculated. Our

findings confirm the presence of a FRET relationship between the blue and green model compounds.

To obtain the FRET data, the absorption and emission spectra of both the donor, blue model compound and the acceptor, green model compound, were recorded. The spectral overlap integral (J) was determined by overlaying the donor's emission spectrum with the acceptor's absorption spectrum (Figure 3-6). Subsequently, the emission spectrum of a donor–acceptor mixture (in a 50:50 ratio) was measured upon excitation at 357 nm, corresponding to the donor's absorption maximum. The emission profile of the mixture exhibited significant quenching of the donor fluorescence, accompanied by an increase and a hypsochromic shift in the acceptor emission (Figure 3-7). These observations are indicative of efficient energy transfer from the donor to the acceptor.[43] Förster radius was determined to be 7.50 nm, calculated using the literature-reported quantum yield of the donor,[31] an assumed dipole orientation factor ($\kappa^2 = 2/3$), and the spectral overlap integral (J). The experimental FRET efficiency (E) was also obtained and used to calculate the donor–acceptor separation distance (r), which was found to be 6.82 nm (see SI for calculations). This value falls well within the 1–10 nm range characteristic of non-radiative Förster-type energy transfer.

Table 3-4: FRET data of blue and green model compounds

Terms	**Values**
Spectral overlap integral, J	$2.90 \times 10^{16}\ M^{-1} \cdot cm^{-1} \cdot nm^4$
Förster radius, R_0	7.50 nm
FRET efficiency, E	63.9 %

Donor-acceptor distance, r	6.82 nm

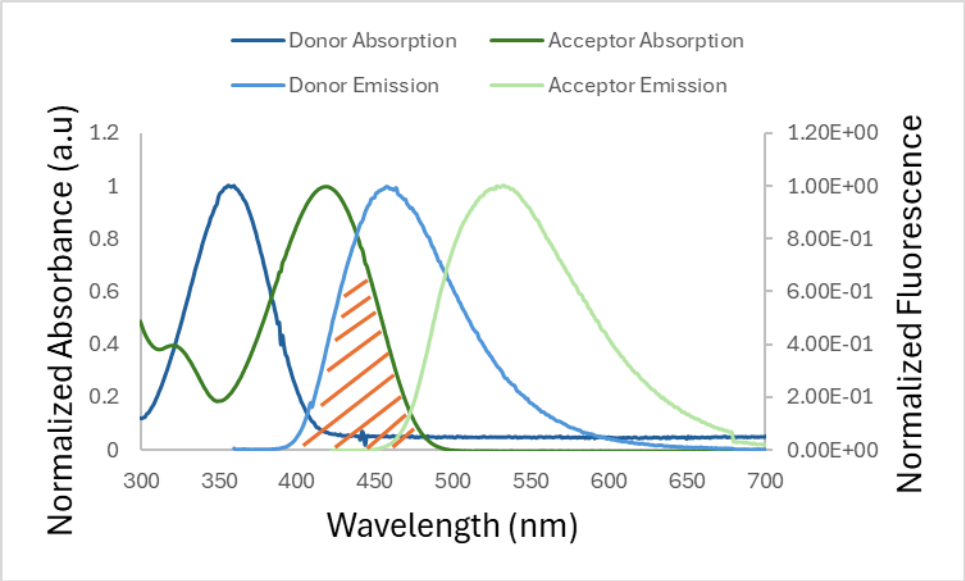

Figure 3-6: Spectral overlap between the blue **1-12** (donor) and green **3-2** (acceptor) model compounds (DCM, $1x10^{-5}$ M).

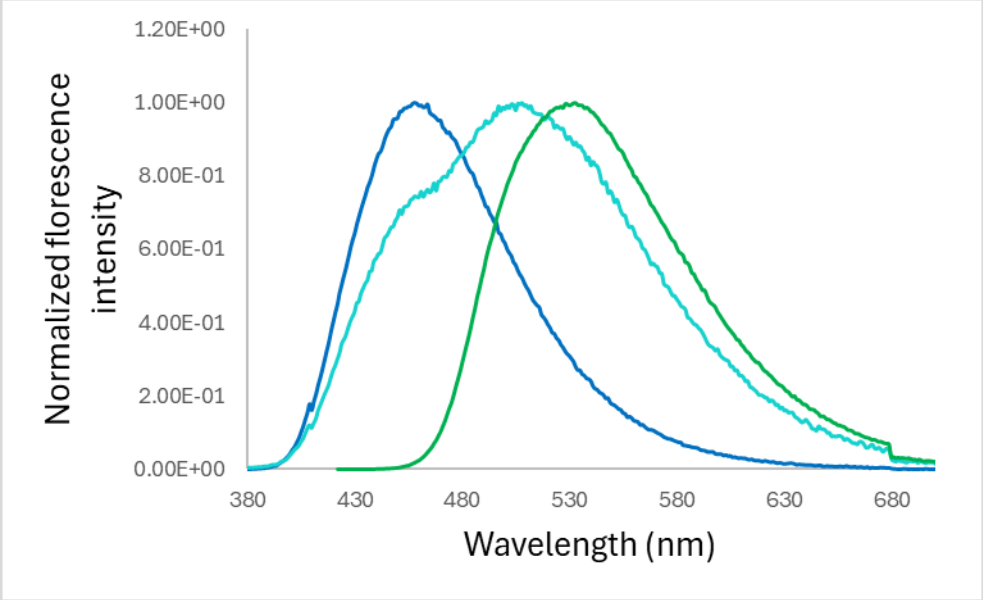

Figure 3-7: Emission spectra of **1-12**, **3-2**, and their mixture in a 50:50 ratio (DCM, $1x10^{-5}$ M).

3.3 Conclusion and Outlook

In summary, this Chapter demonstrated the successful substitution of benzylamine at the phosphorus center of a green-emitting compound to promote self-assembly via hydrogen bonding. In contrast, the same modification proved challenging for the orange-emitting analogue, compound **3-4**, with the associated synthetic limitations discussed in detail. To overcome these difficulties, alternative emitter systems incorporating electron-donating groups, specifically 2-thienyl and 4-methoxyphenyl derivatives, were synthesized using cross-coupling strategies described in Chapter Two. Although benzylamino substitution was attempted on these new systems, purification proved difficult, often leading to decomposition. Despite the challenges associated with **3-4**, it remains a promising candidate for further purification efforts compared to the explored, red-shifted alternatives. Finally, FRET studies between compound **1–12** and the **3-2** emitter successfully provided evidence of energy transfer.

3.4 Experimental Section

3.4.1 General Considerations

The synthesis of **2-1** and reactions with 1 N HCl were conducted under ambient conditions, while all other reactions were carried out under an argon atmosphere using standard Schlenk techniques. *Refer to section 2.4.1 for all other general considerations.*

3.4.2 Synthetic Procedures

Synthesis of **3-2**

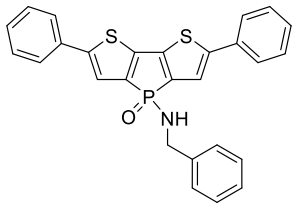

3-2

Compound **2-2** (0.09 g, 0.24 mmol) was treated with hydrochloric acid (2 mL, 1 N) in suspension and stirred overnight. The resulting suspension was filtered, thoroughly washed with water, and air-dried. The dried solid was then transferred to a Schlenk flask, evacuated under vacuum, and suspended in dry DCM (100 mL). With continuous stirring at 0 °C, catalytic DMF (3 drops) and $SOCl_2$ (5 mL) were added. After allowing the reaction mixture to warm to room temperature, stirring continued for an additional hour. Volatile components were subsequently removed under reduced pressure, and the residue was redissolved in DCM. Separately, benzylamine (0.08 mL, 0.73 mmol) was dissolved in 30 mL of dry diethyl ether in a Schlenk flask, cooled in an ice bath with stirring. The DCM solution containing the reactive intermediate was then slowly added to the benzylamine solution, resulting in an immediate color change to green. Once the addition was complete, the mixture was stirred for 1.5 hours at room temperature. The reaction mixture was filtered, and the filtrate was washed with water and dried over anhydrous magnesium sulfate ($MgSO_4$). Final purification was achieved via column chromatography on silica gel

using a 1:1 mixture of ethyl acetate and diethyl ether as eluent, yielding a yellow solid (0.06 g, 56.3%).

$^{31}P\{^{1}H\}$ NMR (162 MHz, $CDCl_3$): δ = 20.4 ppm.

^{1}H NMR (400 MHz, $CDCl_3$) δ = 7.56 – 7.49 (m, 4H), 7.44 – 7.20 (m, 10H), 7.18 (d, *J* = 3.0 Hz, 2H), 4.16 (dd, *J* = 11.8, 7.0 Hz, 2H), 3.21 (d, *J* = 8.5 Hz, 1H).

^{13}C NMR (101 MHz, $CDCl_3$) δ = 148.0 (d, *J* = 15.3 Hz), 143.7 (d, *J* = 28.6 Hz), 139.1 (d, *J* = 5.6 Hz), 137.8 (s), 136.4 (s), 133.5 (s), 129.2 (s), 128.6 (s), 128.3 (s), 127.7 (s), 127.6 (s), 125.7 (s), 121.1 (d, *J* = 14.1 Hz), 44.8 (s).

Theoretical mass: 469.0724 g/mol HRAM MS m/z 470.0796 g/mol

Synthesis of **3-5**

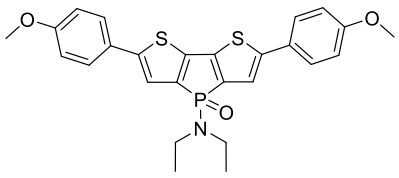

3-5

Compound **2-1** (0.03g, 0.07 mmol), 4-methoxyphenylboronic acid (0.02g, 0.15 mmol), and potassium carbonate (0.08g, 0.58 mmol) were placed in a Schlenk flask, evacuated, and dissolved in dry toluene (25 mL). $[Pd(PPh_3)_4]$ (0.01g, 0.01 mmol) was added swiftly under inert atmosphere, the reflux condenser was fitted back, and 5 mL of water was introduced into the reaction mixture. The reaction was refluxed overnight. Upon

completion, the mixture was cooled, then passed through a celite plug. The crude product was further purified by column chromatography on silica gel using a 1:1 mixture of ethyl acetate and hexanes as the eluent, affording a brown solid (0.03 g, 69.4%).

$^{31}P\{^{1}H\}$ NMR (162 MHz, $CDCl_3$): δ = 23.5 ppm.

^{1}H NMR (400 MHz, $CDCl_3$) δ = 7.53 – 7.44 (m, 2H), 7.16 (d, *J* = 2.9 Hz, 1H), 6.97 – 6.89 (m, 2H), 3.84 (s, 3H), 3.15 (dq, *J* = 12.1, 7.0 Hz, 2H), 1.11 (t, *J* = 7.0 Hz, 3H).

^{13}C NMR (101 MHz, $CDCl_3$) δ = 159.7 (s), 147.6 (d, *J* = 15.3 Hz), 142.8 (d, *J* = 27.6 Hz), 138.0 (s), 136.7 (s), 131.4 (s), 128.2 (s), 127.0 (s), 126.5 (s), 119.9 (d, *J* = 14.0 Hz), 114.5 (s), 77.2 (s), 55.4 (s), 38.5 (d, *J* = 5.4 Hz), 14.4 (d, *J* = 2.7 Hz).

Theoretical mass: 495.1092 g/mol HRAM MS m/z 496.1167 g/mol

Synthesis of **3-6**

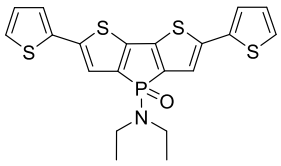

3-6

Compound **2-1** (0.04 g, 0.10 mmol), 2-thiopheneboronic acid pinacol ester (0.04g, 0.20 mmol), and potassium carbonate (0.11g, 0.78 mmol) were placed in a Schlenk flask, evacuated, and dissolved in dry tetrahydrofuran (THF). $[Pd(PPh_3)_4]$ (0.01g, 0.01 mmol) was added swiftly under inert atmosphere, the reflux condenser was fitted back, and 5 mL of water was introduced into the reaction mixture. The reaction was refluxed overnight. Upon completion, the mixture was cooled, then passed through a celite plug. The crude

product was further purified by column chromatography on silica gel using a 1:1 mixture of ethyl acetate and hexanes as the eluent, affording a brown solid (0.03 g, 73.7%).

$^{31}P\{^{1}H\}$ NMR (162 MHz, $CDCl_3$): δ = 22.4 ppm.

^{1}H NMR (400 MHz, $CDCl_3$) δ = 7.27 (d, *J* = 1.1 Hz, 1H), 7.21 – 7.11 (m, 4H), 7.04 (dd, *J* = 5.1, 3.6 Hz, 2H), 3.14 (dq, *J* = 12.2, 7.1 Hz, 4H), 1.11 (t, *J* = 7.1 Hz, 6H).

^{13}C NMR (101 MHz, $CDCl_3$) δ = 142.8 (d, *J* = 27.4 Hz), 140.8 (d, *J* = 16.2 Hz), 138.4 (s), 137.1 (s), 136.3 (s), 128.1(s), 124.8 (d, *J* = 98.6 Hz), 121.5 (d, *J* = 14.2 Hz), 38.5 (d, *J* = 5.4 Hz), 14.4 (d, *J* = 2.6 Hz).

Chapter Four: Conclusions and Outlook

4.1 Conclusions

The overall goal of this thesis is to document efforts to synthesize model compounds for self-assembled dithienophosphole-based phosphinamides. The long-term objective is to incorporate these materials into the emitting layer of WOLEDs. Since the complete set of blue species, including emitter, model compound, and liquid crystal, has already been synthesized, this thesis focused on developing the corresponding green and orange species. Chapter Two details the synthesis of the brominated precursor **2-1**, along with the green (**2-2**) and orange (**2-3**) emitters. Characterization involved analyzing their optical properties via absorption and emission spectroscopy that also revealed their extinction coefficients and Stokes shifts. Finally, density functional theory (DFT) calculations were used to gain deeper insight into their electronic structures and photophysical behavior. Results of photophysical analysis revealed that the brominated precursor exhibited a single excitation transition, while the others showed two distinct excitation transitions, reflecting their increased conjugation. The measured Stokes shifts followed a clear linear trend and were substantially larger than those observed in previously reported analogues. Although some variation was noted in the extinction coefficients, these differences were attributed to the electron-donating properties and conformational flexibility of the dimethylamine substituent. Overall, the synthesized compounds successfully exhibited the desired emission colors.

In Chapter Three, the synthesis of model compounds derived from the green and orange emitters is presented. While the synthesis of the green model compound was successful, the preparation of the orange model compound posed significant challenges. To address this, alternative emitters incorporating 2-thienyl and 4-methoxyphenyl electron-donating substituents were targeted to develop their corresponding model systems. However, subsequent benzylamino substitution at the phosphorus center in these new systems also proved difficult. Characterization of the successfully synthesized compounds included optical property analysis, such as absorption and emission spectra, extinction coefficients, and Stokes shifts. The results of the optical analysis followed similar trends with those observed for the π-extended systems discussed in Chapter Two. Additionally, DFT calculations were employed to further elucidate their electronic structures. Lastly, Förster Resonance Energy Transfer (FRET) studies were conducted between the previously reported blue model emitter **1-12** and the newly synthesized green model compound **3-2** that confirmed their potential for energy transfer in multi-emitter systems. The results confirmed the occurrence of energy transfer between the two compounds, as evidenced by donor fluorescence quenching and a corresponding enhancement in acceptor emission.

4.2 Outlook

4.2.1 Synthetic Future Works

To complete the model compound series, successful purification of the orange model compound **3-4** remains essential. Based on the synthetic evidence presented in Chapter Three and comparisons with other electron-donating emitters, **3-4** continues to be the

most promising candidate to serve as the final bathochromic model compound. One potential strategy to achieve this involves recrystallization using a non-polar solvent while strictly avoiding protic solvents. Additionally, given that this compound is prone to degradation in diethyl ether, solvents with similar properties, such as tetrahydrofuran (THF), should also be excluded from the purification process.

Another important future goal is to grow single crystals of the successfully synthesized compounds, particularly the model compounds bearing PONH moiety, and their mixtures. Single-crystal X-ray diffraction would enable direct observation of molecular packing and hydrogen bonding interactions, offering valuable insights into their self-assembly behavior in the solid state. Understanding these interactions is critical for evaluating their potential in optoelectronic applications, especially when comparing their structural organization to that of the previously reported blue model compound. Such comparisons could reveal trends in molecular alignment, stacking motifs, and intermolecular forces that influence their bulk material properties.

In line with the blue-emitting series, another key future objective is the synthesis of liquid crystals with the green and orange emitters. Fortunately, the synthetic route to these liquid crystal derivatives closely parallels that are used for the corresponding model compounds. Therefore, once a reliable and reproducible procedure is established for the orange model compound, the synthesis of its liquid crystalline analog should proceed through similar steps. Likewise, the green liquid crystal is expected to follow the same synthetic strategy as the green model compound (Scheme 4-1). Achieving this will complete the set of color-tuned liquid crystalline materials, enabling further investigation into their alignment,

mesophase behavior, and suitability for applications in tunable light-emitting devices such as WOLEDs.

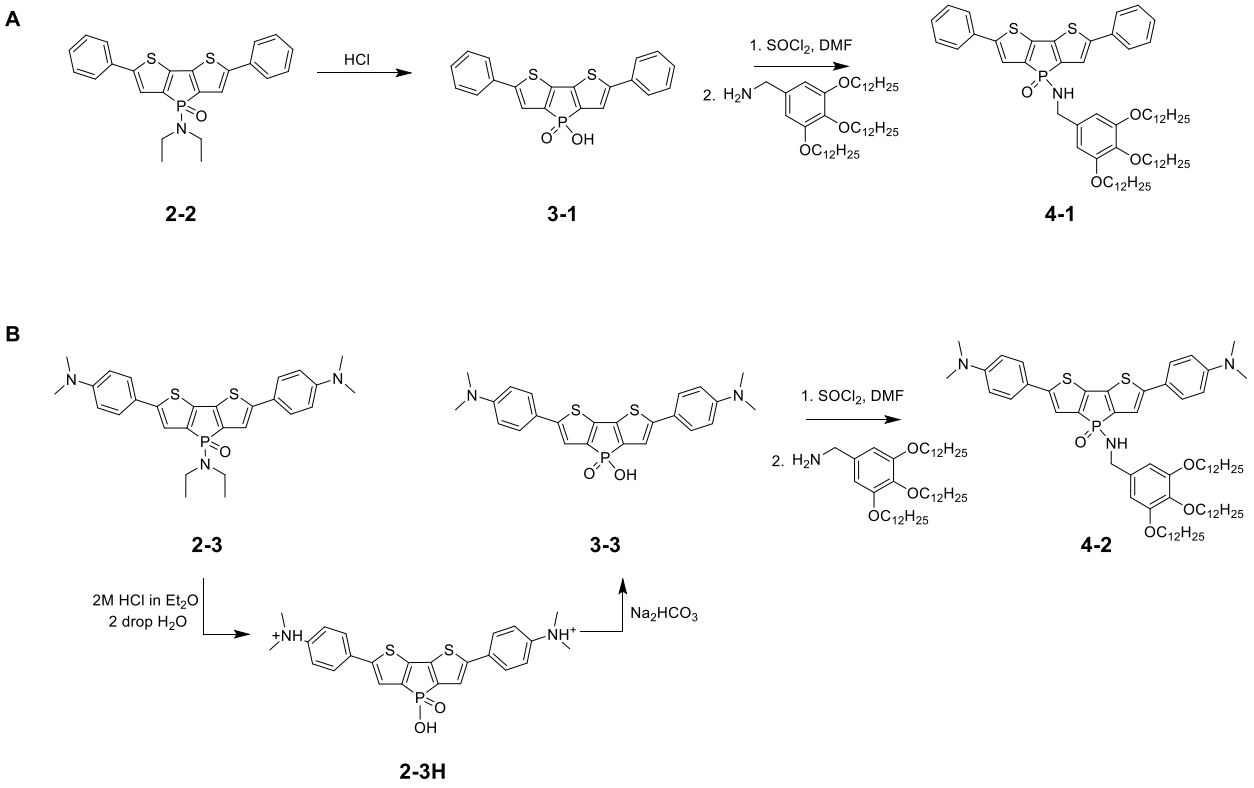

Scheme 4-1: Proposed synthetic pathway for green and orange dithienophosphile-based phosphinamide liquid crystals.

4.2.2 Time-Dependent Density Functional Theory (TD-DFT) and FRET Studies

Time-Dependent Density Functional Theory (TD-DFT) is an extension of Density Functional Theory (DFT) that enables the calculation of time-dependent properties of molecules, including electronic excitations, optical absorption spectra, and other excited-state phenomena.[44] TD-DFT can be employed to compute and/or compare the absorption spectra of all addressed compounds in this thesis. This computational approach will be particularly valuable for compounds that could not be fully purified, as it will provide

theoretical insight into their electronic transitions and support experimental observations where direct measurements may be limited.[45]

Once compound **3-4** is successfully isolated and purified, comprehensive Förster Resonance Energy Transfer (FRET) studies involving all three emitters, blue, green, and orange, can be conducted. These studies will provide critical insights into the efficiency and directionality of energy transfer between the compounds, which is essential for evaluating their compatibility in a WOLED system. In addition to energy transfer dynamics, these FRET investigations can offer valuable information about intermolecular interactions, particularly hydrogen bonding and other supramolecular arrangements. Since the model compounds contain the PONH moiety, capable of forming hydrogen bonds, FRET behavior can reflect how these interactions influence molecular packing, aggregation, and spatial proximity, all of which are crucial for self-assembly. Observing shifts in FRET efficiency or spectral behavior under different conditions may also reveal how non-covalent interactions modulate the optical and electronic properties of the system.[42] The same studies could also be done for the liquid crystal compound series once fully synthesized, This deeper understanding of both photophysical behavior and supramolecular architecture will guide the rational design of self-assembling materials for next-generation optoelectronic applications.

5. References

(1) Mateo-Alonso, A. π-Conjugated Materials: Here, There, and Everywhere. *Chem. Mater.* **2023**, *35* (4), 1467–1469. https://doi.org/10.1021/acs.chemmater.2c03567.

(2) Facchetti, A. π-Conjugated Polymers for Organic Electronics and Photovoltaic Cell Applications. *Chem. Mater.* **2011**, *23* (3), 733–758. https://doi.org/10.1021/cm102419z.

(3) Tuncel, D. π-Conjugated Nanostructured Materials: Preparation, Properties and Photonic Applications. *Nanoscale Adv.* **2019**, *1* (1), 19–33. https://doi.org/10.1039/C8NA00108A.

(4) Günes, S.; Neugebauer, H.; Sariciftci, N. S. Conjugated Polymer-Based Organic Solar Cells. *Chem. Rev.* **2007**, *107* (4), 1324–1338. https://doi.org/10.1021/cr050149z.

(5) Seo, D.-K.; Hoffmann, R. Direct and Indirect Band Gap Types in One-Dimensional Conjugated or Stacked Organic Materials. *Theor. Chem. Acc.* **1999**, *102* (1), 23–32. https://doi.org/10.1007/s002140050469.

(6) Zou, S.-J.; Shen, Y.; Xie, F.-M.; Chen, J.-D.; Li, Y.-Q.; Tang, J.-X. Recent Advances in Organic Light-Emitting Diodes: Toward Smart Lighting and Displays. *Mater. Chem. Front.* **2020**, *4* (3), 788–820. https://doi.org/10.1039/C9QM00716D.

(7) Kitai, A. *Principles of Solar Cells, LEDs and Related Devices: The Role of the PN Junction*, 1st ed.; Wiley, 2018. https://doi.org/10.1002/9781119450986.

(8) Thejokalyani, N.; Dhoble, S. J. Novel Approaches for Energy Efficient Solid State Lighting by RGB Organic Light Emitting Diodes – A Review. *Renew. Sustain. Energy Rev.* **2014**, *32*, 448–467. https://doi.org/10.1016/j.rser.2014.01.013.

(9) Reineke, S.; Thomschke, M.; Lüssem, B.; Leo, K. White Organic Light-Emitting Diodes: Status and Perspective. *Rev. Mod. Phys.* **2013**, *85* (3), 1245–1293. https://doi.org/10.1103/RevModPhys.85.1245.

(10) *CIE 1931 | Avery Dennison*. https://label.averydennison.com (accessed 2025-07-22).

(11) He, Z.; Zhao, W.; Lam, J. W. Y.; Peng, Q.; Ma, H.; Liang, G.; Shuai, Z.; Tang, B. Z. White Light Emission from a Single Organic Molecule with Dual Phosphorescence at Room Temperature. *Nat. Commun.* **2017**, *8* (1), 416. https://doi.org/10.1038/s41467-017-00362-5.

(12) Nyakuchena, J.; Chiromo, H.; Radpour, S.; Guckenburg, J.; Huang, J. Additive Mixing of Emissive Ligands in Covalent Organic Frameworks for White Light Emission. *ACS Appl. Mater. Interfaces* **2024**. https://doi.org/10.1021/acsami.4c09728.

(13) Valeur, B.; Berberan-Santos, M. N. *Molecular Fluorescence: Principles and Applications*, 1st ed.; Wiley, 2012. https://doi.org/10.1002/9783527650002.

(14) Thejo Kalyani, N.; Dhoble, S. J. Novel Materials for Fabrication and Encapsulation of OLEDs. *Renew. Sustain. Energy Rev.* **2015**, *44*, 319–347. https://doi.org/10.1016/j.rser.2014.11.070.

(15) Lee, M.-T.; Yen, C.-K.; Yang, W.-P.; Chen, H.-H.; Liao, C.-H.; Tsai, C.-H.; Chen, C. H. Efficient Green Coumarin Dopants for Organic Light-Emitting Devices. *Org. Lett.* **2004**, *6* (8), 1241–1244. https://doi.org/10.1021/ol049903d.

(16) Pochan, D.; Scherman, O. Introduction: Molecular Self-Assembly. *Chem. Rev.* **2021**, *121* (22), 13699–13700. https://doi.org/10.1021/acs.chemrev.1c00884.
(17) Whitesides, G. M.; Grzybowski, B. Self-Assembly at All Scales. *Science* **2002**, *295* (5564), 2418–2421. https://doi.org/10.1126/science.1070821.
(18) Dückert, H.; Pries, V.; Khedkar, V.; Menninger, S.; Bruss, H.; Bird, A. W.; Maliga, Z.; Brockmeyer, A.; Janning, P.; Hyman, A.; Grimme, S.; Schürmann, M.; Preut, H.; Hübel, K.; Ziegler, S.; Kumar, K.; Waldmann, H. Natural Product–Inspired Cascade Synthesis Yields Modulators of Centrosome Integrity. *Nat. Chem. Biol.* **2012**, *8* (2), 179–184. https://doi.org/10.1038/nchembio.758.
(19) Magalhães, M. I.; Almeida, A. P. C. Nature-Inspired Cellulose-Based Active Materials: From 2D to 4D. *Appl. Biosci.* **2023**, *2* (1), 94–114. https://doi.org/10.3390/applbiosci2010009.
(20) Guldin, S. Self-Assembly of Soft Matter. In *Inorganic Nanoarchitectures by Organic Self-Assembly*; Guldin, S., Ed.; Springer Theses; Springer International Publishing: Heidelberg, 2013; pp 1–17. https://doi.org/10.1007/978-3-319-00312-2_1.
(21) Wang, C.; Chen, Q.; Sun, F.; Zhang, D.; Zhang, G.; Huang, Y.; Zhao, R.; Zhu, D. Multistimuli Responsive Organogels Based on a New Gelator Featuring Tetrathiafulvalene and Azobenzene Groups: Reversible Tuning of the Gel−Sol Transition by Redox Reactions and Light Irradiation. *J. Am. Chem. Soc.* **2010**, *132* (9), 3092–3096. https://doi.org/10.1021/ja910721s.
(22) Kuzina, M. A.; Kartsev, D. D.; Stratonovich, A. V.; Levkin, P. A. Organogels versus Hydrogels: Advantages, Challenges, and Applications. *Adv. Funct. Mater.* **2023**, *33* (27), 2301421. https://doi.org/10.1002/adfm.202301421.
(23) Bisoyi, H. K.; Li, Q. Liquid Crystals: Versatile Self-Organized Smart Soft Materials. *Chem. Rev.* **2022**, *122* (5), 4887–4926. https://doi.org/10.1021/acs.chemrev.1c00761.
(24) Climent-Ezquerra, B.; Guillén-González, F. A Review of Mathematical Analysis of Nematic and Smectic-A Liquid Crystal Models. *Eur. J. Appl. Math.* **2014**, *25* (1), 133–153. https://doi.org/10.1017/S0956792513000338.
(25) Sharma, A.; Magrini, M.; Han, Y.; Walba, D. M.; Majumdar, A.; Lagerwall, J. P. F. How Smectic-A and Smectic-C Liquid Crystals Resolve Confinement-Induced Frustration in Spherical Shells. *Soft Matter* **2024**, *20* (48), 9586–9596. https://doi.org/10.1039/D4SM01263A.
(26) Sun, D.; Saxena, R.; Fan, X.; Athanasopoulos, S.; Duda, E.; Zhang, M.; Bagnich, S.; Zhang, X.; Zysman-Colman, E.; Köhler, A. Regiochemistry of Donor Dendrons Controls the Performance of Thermally Activated Delayed Fluorescence Dendrimer Emitters for High Efficiency Solution-Processed Organic Light-Emitting Diodes. *Adv. Sci.* **2022**, *9* (20), 2201470. https://doi.org/10.1002/advs.202201470.
(27) Hadjichristov, G. B.; Marinov, Y. G. Photoluminescent Thin Films of Room-Temperature Glassy Tris(Keto-Hydrozone) Discotic Liquid Crystals and Their Nanocomposites with Single-Walled Carbon Nanotubes for Optoelectronics. *ACS Omega* **2023**, *8* (30), 27102–27116. https://doi.org/10.1021/acsomega.3c02103.
(28) Zhang, C.; Yan, H.; He, Y.; Chai, Y.; Zhou, D. Thermally Activated Delayed Fluorescence Dendrimers Achieving 20% External Quantum Efficiency for Solution-

Processed OLEDs. *Mater. Chem. Front.* **2022**, *6* (22), 3442–3449. https://doi.org/10.1039/D2QM00833E.
(29) Mathey, F. The Organic Chemistry of Phospholes. *Chem. Rev.* **1988**, *88* (2), 429–453. https://doi.org/10.1021/cr00084a005.
(30) He, X.; Lin, J.; Kan, W. H.; Dong, P.; Trudel, S.; Baumgartner, T. Molecular Engineering of "Click"-Phospholes Towards Self-Assembled Luminescent Soft Materials. *Adv. Funct. Mater.* **2014**, *24* (7), 897–906. https://doi.org/10.1002/adfm.201302294.
(31) Wang, Z.; Gelfand, B. S.; Baumgartner, T. Dithienophosphole-Based Phosphinamides with Intriguing Self-Assembly Behavior. *Angew. Chem. Int. Ed.* **2016**, *55* (10), 3481–3485. https://doi.org/10.1002/anie.201511171.
(32) Romero-Nieto, C.; Baumgartner, T. Dithieno[3,2-b:2',3'-d]Phospholes: A Look Back at the First Decade. *Synlett* **2013**, *24* (08), 920–937. https://doi.org/10.1055/s-0032-1317804.
(33) Baumgartner, T.; Neumann, T.; Wirges, B. The Dithieno[3,2- *b* :2',3'- *d*]Phosphole System: A Novel Building Block for Highly Luminescent π-Conjugated Materials. *Angew. Chem. Int. Ed.* **2004**, *43* (45), 6197–6201. https://doi.org/10.1002/anie.200461301.
(34) Dienes, Y.; Durben, S.; Kárpáti, T.; Neumann, T.; Englert, U.; Nyulászi, L.; Baumgartner, T. Selective Tuning of the Band Gap of π-Conjugated Dithieno[3,2-b:2',3'-d]Phospholes toward Different Emission Colors. *Chem. – Eur. J.* **2007**, *13* (26), 7487–7500. https://doi.org/10.1002/chem.200700399.
(35) Huynh, H. V.; He, X.; Baumgartner, T. Halochromic Generation of White Light Emission Using a Single Dithienophosphole Luminophore. *Chem. Commun.* **2013**, *49* (43), 4899–4901. https://doi.org/10.1039/C3CC41510D.
(36) Wang, Z.; Baumgartner, T. Organophosphorus Avenues toward Self-Assembled Conjugated Soft Materials. *Chem. Rec.* **2015**, *15* (1), 199–217. https://doi.org/10.1002/tcr.201402061.
(37) Samorí, P.; Feng, X.; Bonifazi, D. π-Conjugated Molecules: From Structure to Function. *ChemPlusChem* **2019**, *84* (9), 1177–1178. https://doi.org/10.1002/cplu.201900442.
(38) J. Lennox, A. J.; C. Lloyd-Jones, G. Selection of Boron Reagents for Suzuki–Miyaura Coupling. *Chem. Soc. Rev.* **2014**, *43* (1), 412–443. https://doi.org/10.1039/C3CS60197H.
(39) Romero-Nieto, C.; Durben, S.; Kormos, I. M.; Baumgartner, T. Simple and Efficient Generation of White Light Emission From Organophosphorus Building Blocks. *Adv. Funct. Mater.* **2009**, *19* (22), 3625–3631. https://doi.org/10.1002/adfm.200901540.
(40) Sahoo, H. Förster Resonance Energy Transfer – A Spectroscopic Nanoruler: Principle and Applications. *J. Photochem. Photobiol. C Photochem. Rev.* **2011**, *12* (1), 20–30. https://doi.org/10.1016/j.jphotochemrev.2011.05.001.
(41) Mayoral, M. J.; Serrano-Molina, D.; Camacho-García, J.; Magdalena-Estirado, E.; Blanco-Lomas, M.; Fadaei, E.; González-Rodríguez, D. Understanding Complex Supramolecular Landscapes: Non-Covalent Macrocyclization Equilibria Examined by

Fluorescence Resonance Energy Transfer. *Chem. Sci.* **2018**, *9* (40), 7809–7821. https://doi.org/10.1039/C8SC03229G.
(42) Basak, D.; Das, A.; Ghosh, S. Hydrogen-Bonding Driven Luminescent Assembly and Efficient Förster Resonance Energy Transfer (FRET) in a Dialkoxynaphthalene-Based Organogel. *RSC Adv* **2014**, *4* (82), 43564–43571. https://doi.org/10.1039/C4RA08920K.
(43) Wu, L.; Huang, C.; P. Emery, B.; C. Sedgwick, A.; D. Bull, S.; He, X.-P.; Tian, H.; Yoon, J.; L. Sessler, J.; D. James, T. Förster Resonance Energy Transfer (FRET)-Based Small-Molecule Sensors and Imaging Agents. *Chem. Soc. Rev.* **2020**, *49* (15), 5110–5139. https://doi.org/10.1039/C9CS00318E.
(44) Marques, M. A. L.; Gross, E. K. U. TIME-DEPENDENT DENSITY FUNCTIONAL THEORY. *Annu. Rev. Phys. Chem.* **2004**, *55* (1), 427–455. https://doi.org/10.1146/annurev.physchem.55.091602.094449.
(45) De La Peña O'Shea, Victor. A.; Capel-Sanchez, M.; Blanco-Brieva, G.; Campos-Martin, J. M.; Fierro, J. L. G. The Usefulness of Time-Dependent Density Functional Theory to Describe the Electronic Spectra of Ti-Containing Catalysts. *Angew. Chem. Int. Ed.* **2003**, *42* (47), 5851–5854. https://doi.org/10.1002/anie.200351452.

6. Supplementary Information

6.1 FRET Calculation[13]

Spectral Overlap Integral

$$J = \int F_D(\lambda)\varepsilon_A(\lambda)\lambda^4 d\lambda$$

F_D = normalized fluorescence of the donor only

ε_A = extinction coefficient of the acceptor

λ = wavelength (nm)

Förster Radius

$$R_0 = 0.02108(\kappa^2\eta^{-4}\Phi_D J)^{\frac{1}{6}}$$

κ = orientation factor (2/3)

η = refraction index of DCM

Φ = quantum yield of donor

J = spectral overlap integral

FRET Efficiency

$$E = 1 - \frac{I_{DA}}{I_D}$$

I_{DA} = intensity of donor in mixture

I_D = intensity of donor only

Donor-acceptor radius

$$r = R_0 \left(\frac{1-E}{E}\right)^{1/6}$$

6.2 NMR Spectra

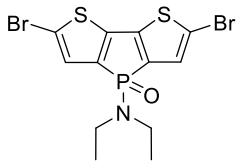

2-1

$^{31}P\{^{1}H\}$ NMR spectroscopy

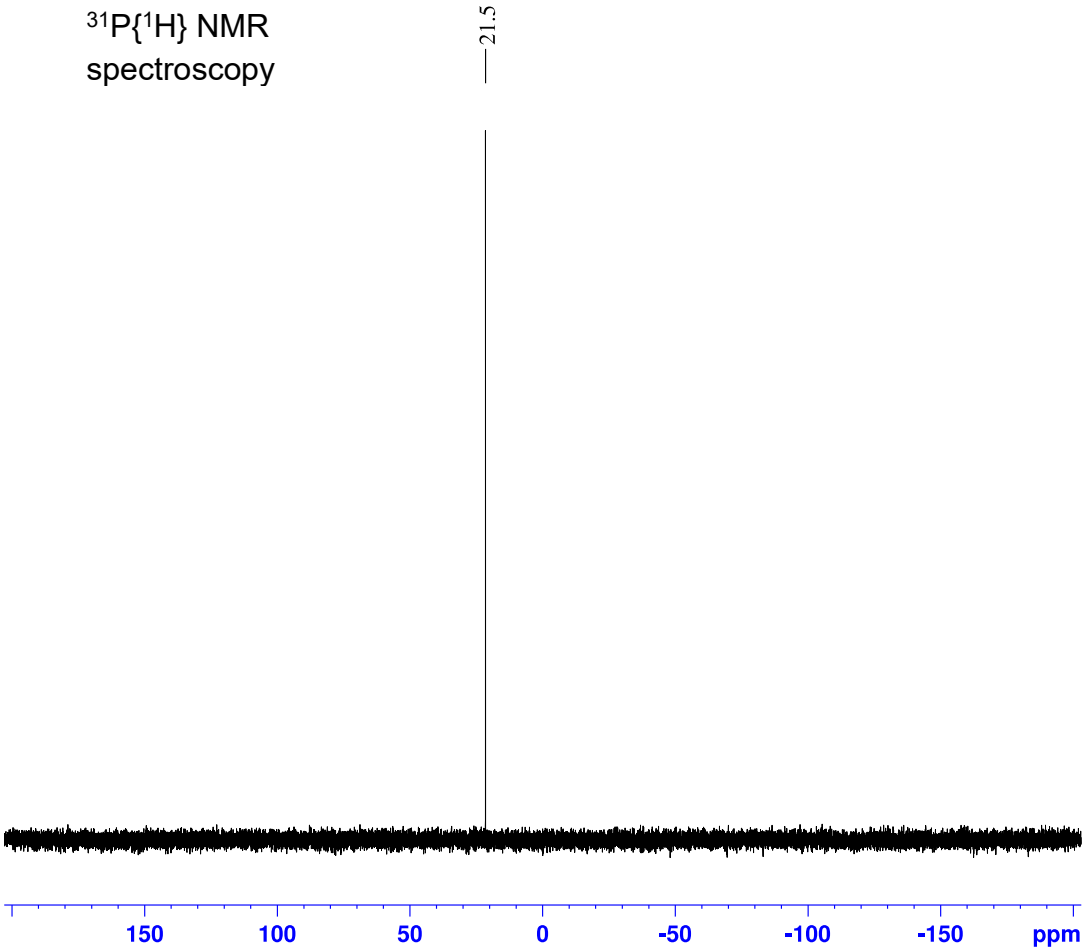

^{1}H NMR spectroscopy

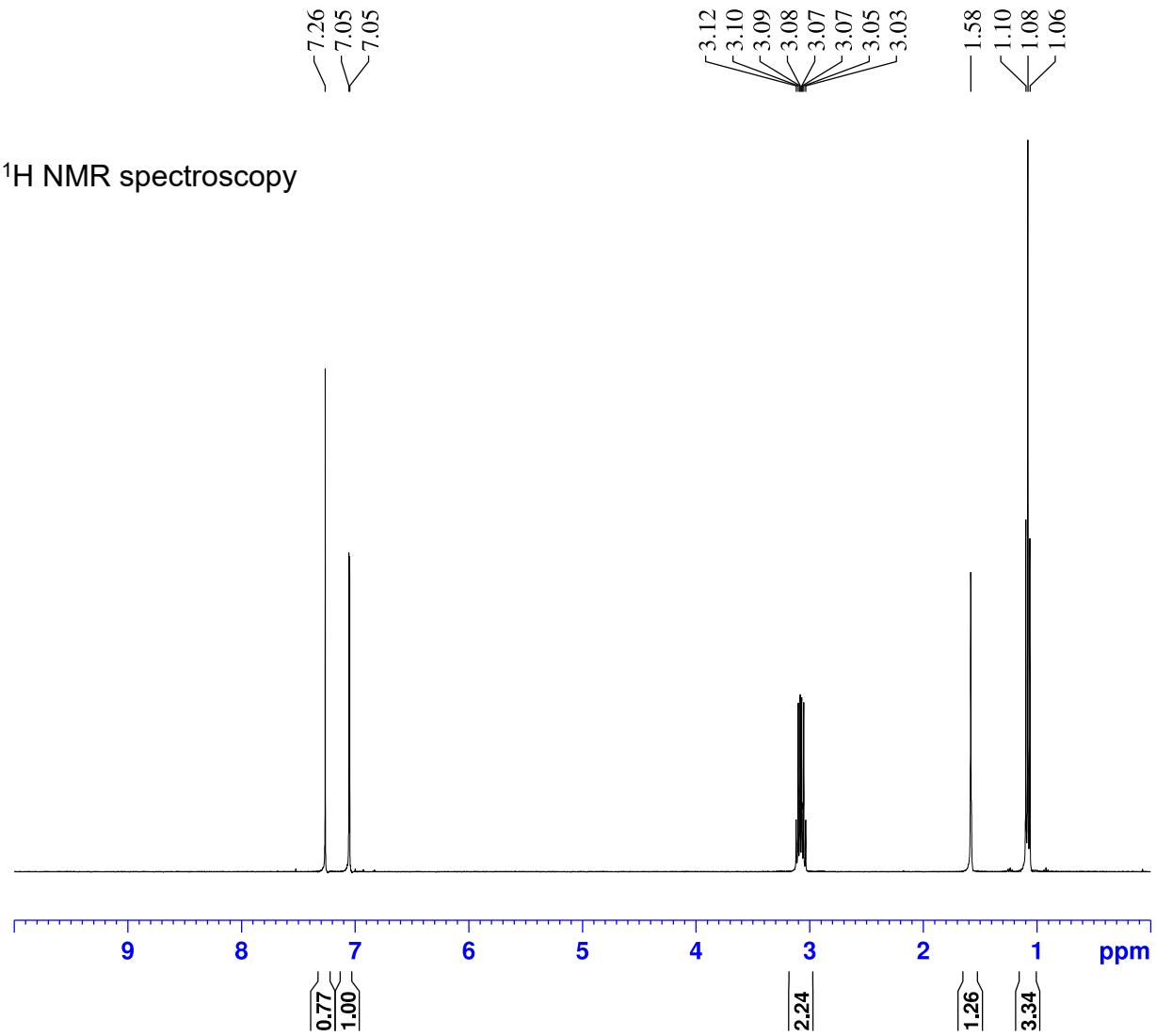

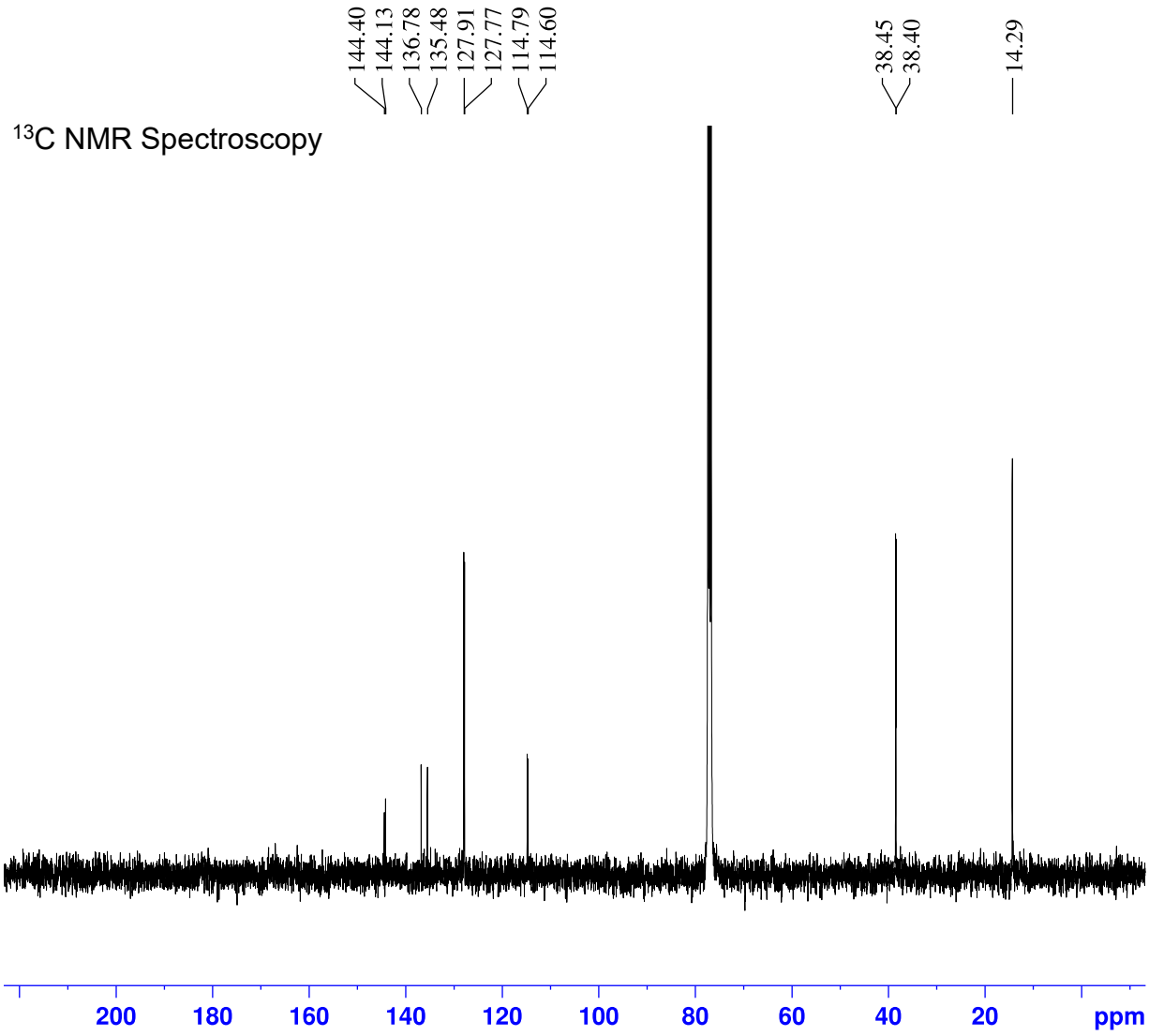
144.40
144.13
136.78
135.48
127.91
127.77
114.79
114.60
38.45
38.40
14.29
13C NMR Spectroscopy
200
180
160
140
120
100
80
60
40
20
ppm

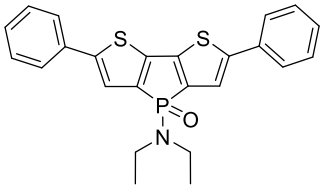

2-2

$^{31}P\{^{1}H\}$ NMR spectroscopy

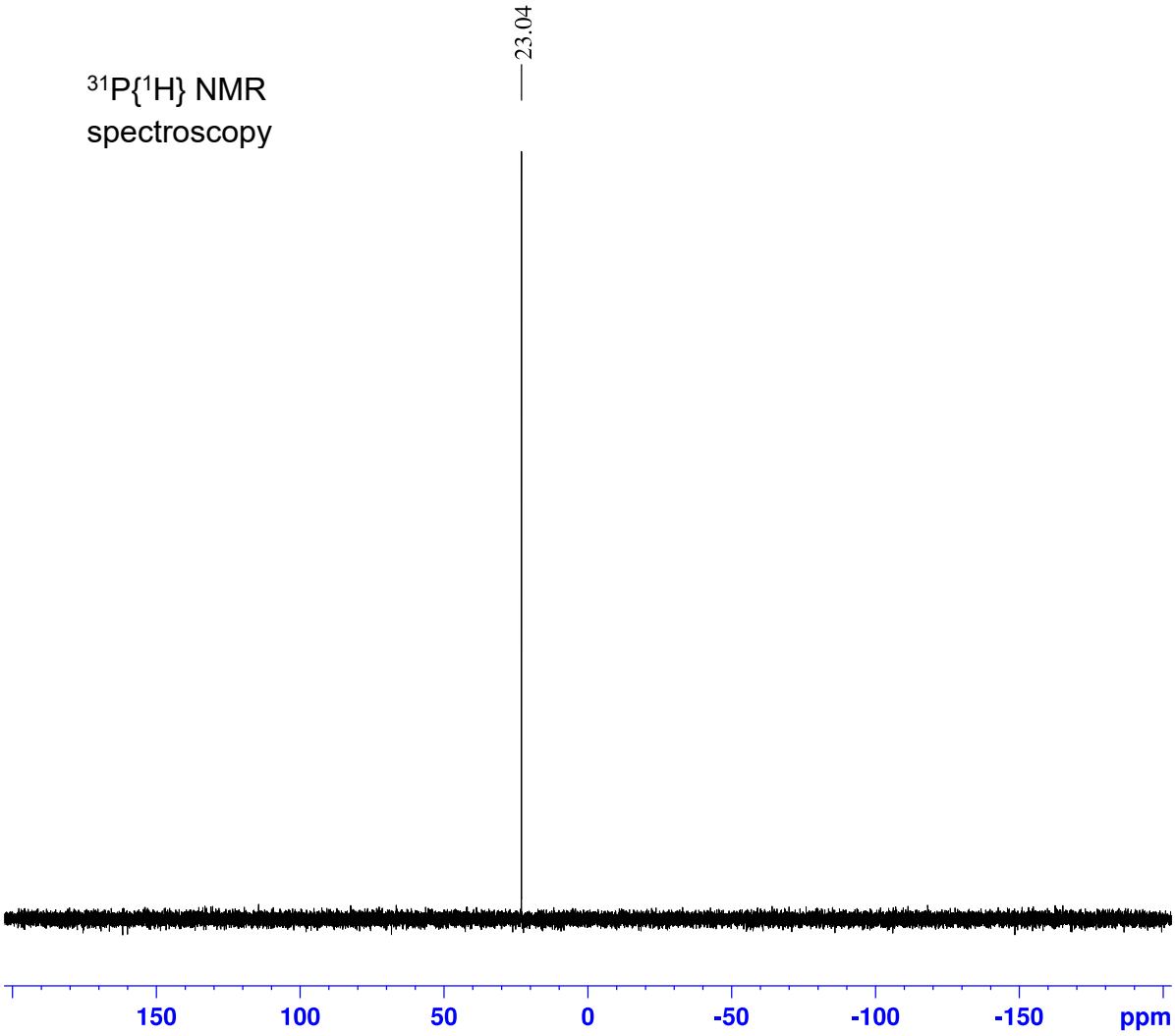

^{1}H NMR spectroscopy

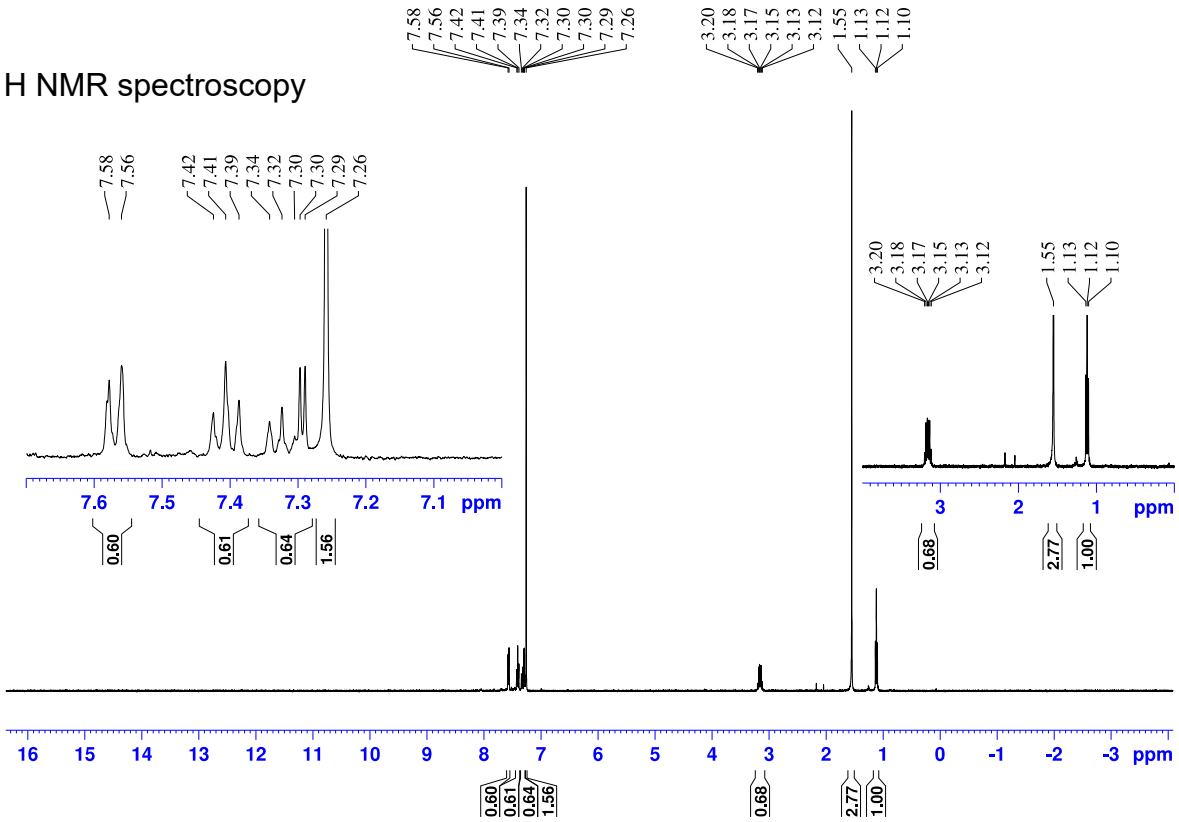

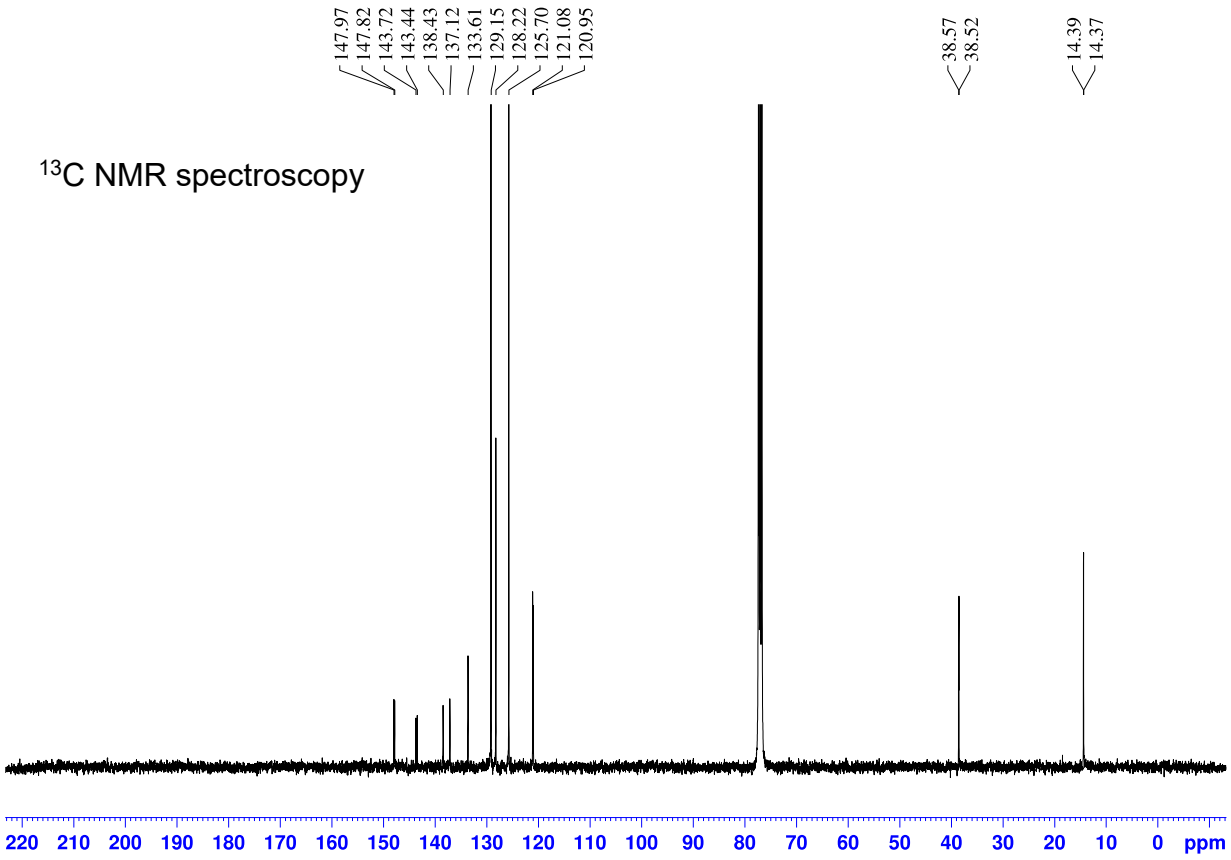
147.97
147.82
143.72
143.44
138.43
137.12
133.61
129.15
128.22
125.70
121.08
120.95
38.57
38.52
14.39
14.37
13C NMR spectroscopy
220 210 200 190 180 170 160 150 140 130 120 110 100 90 80 70 60 50 40 30 20 10 0 ppm

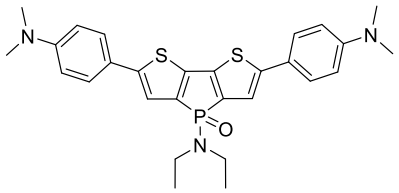

2-3

$^{31}P\{^{1}H\}$ NMR spectroscopy

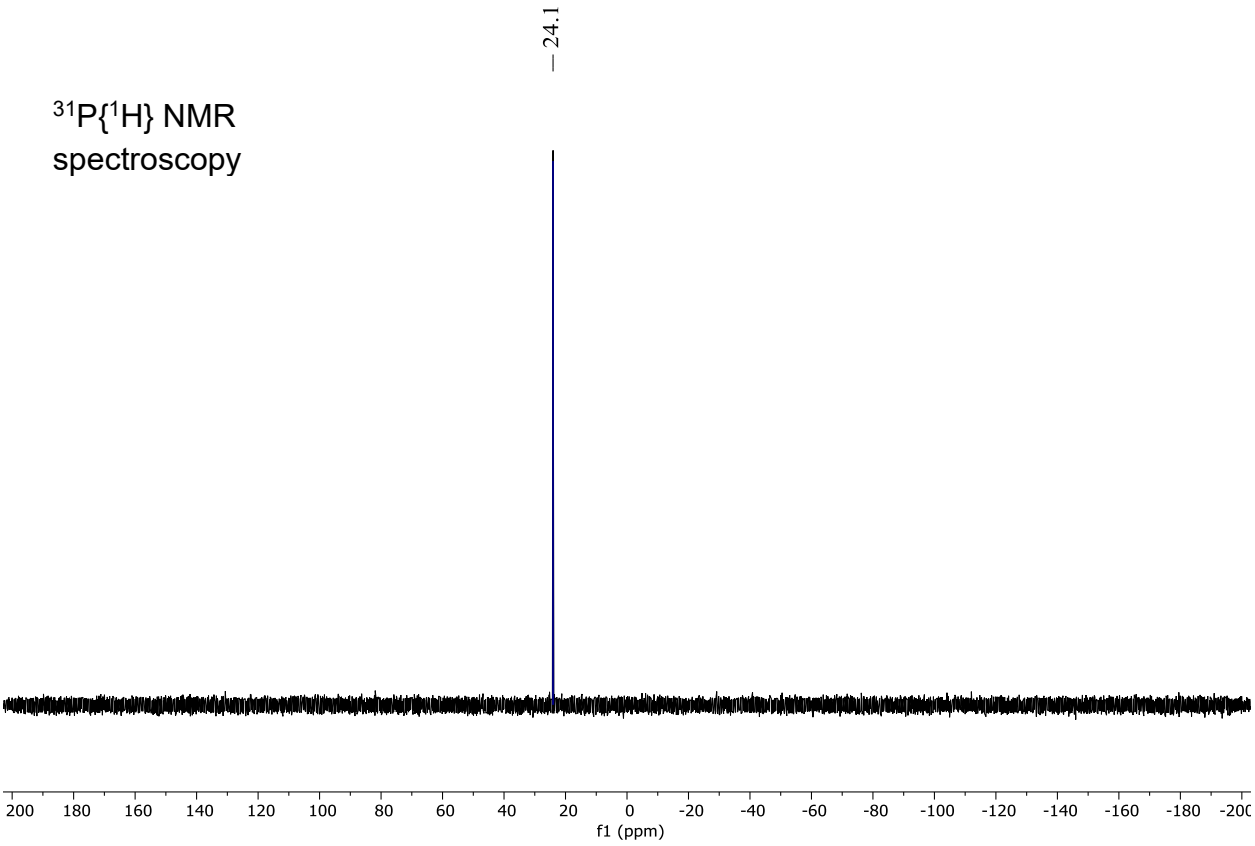

^{1}H NMR spectroscopy

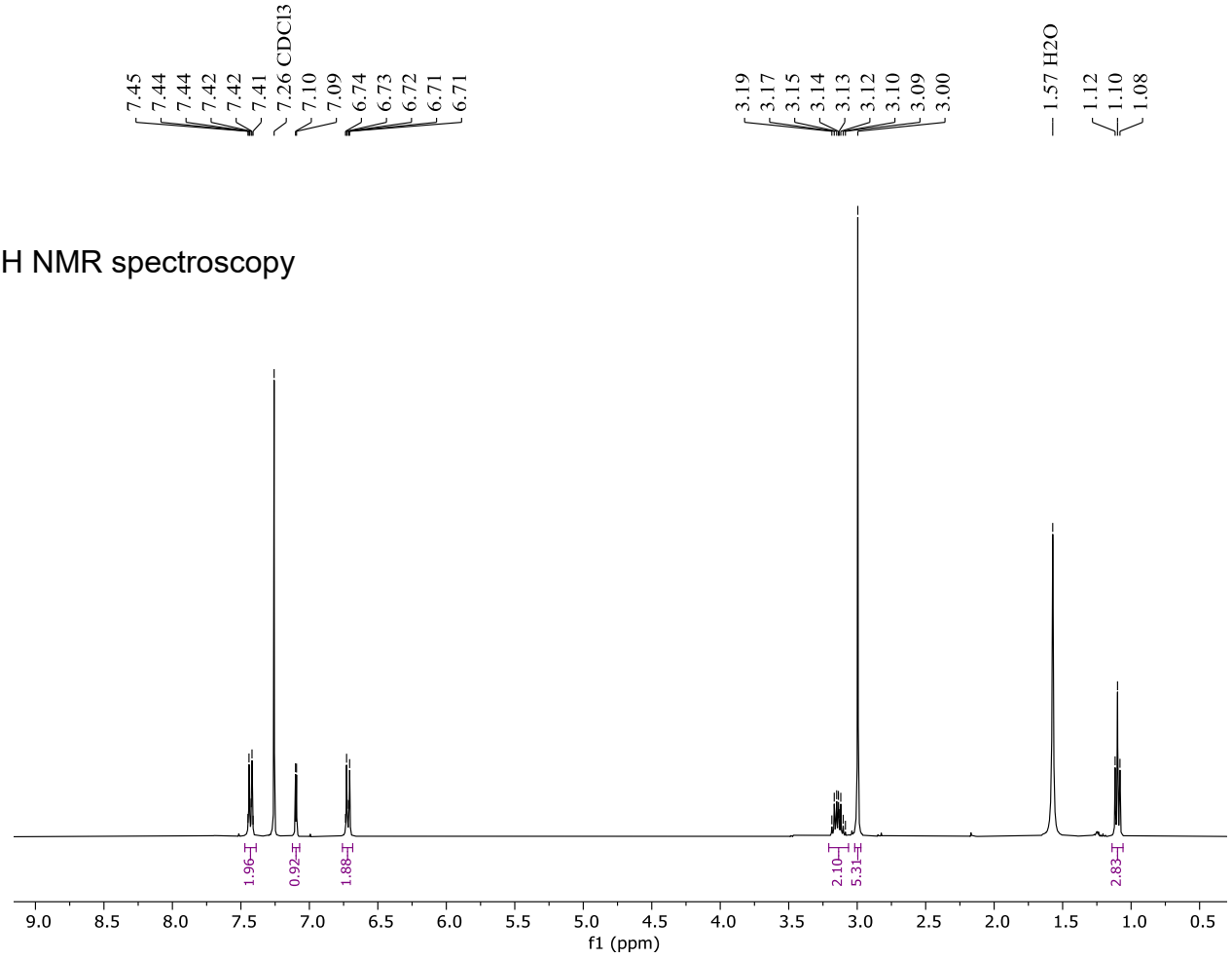

^{13}C NMR spectroscopy

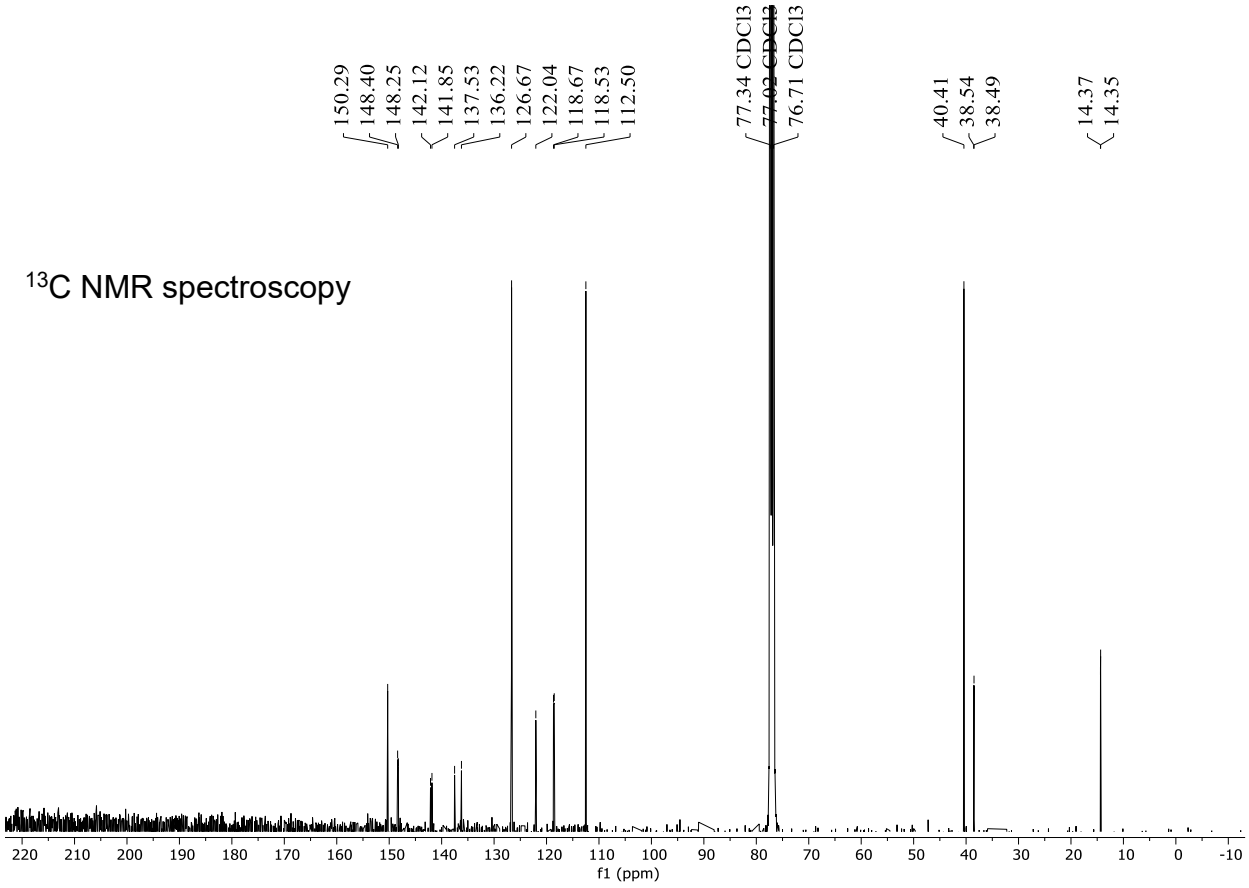

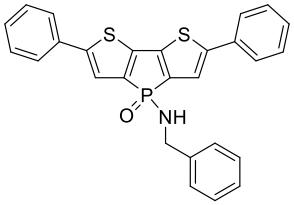

3-2

— 20.4

$^{31}P\{^{1}H\}$ NMR spectroscopy

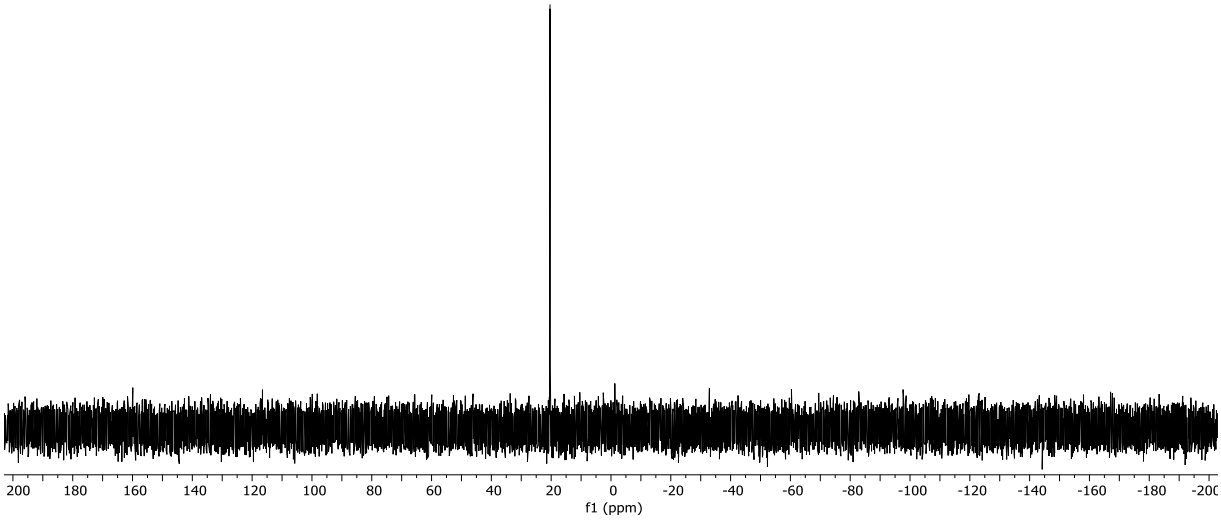

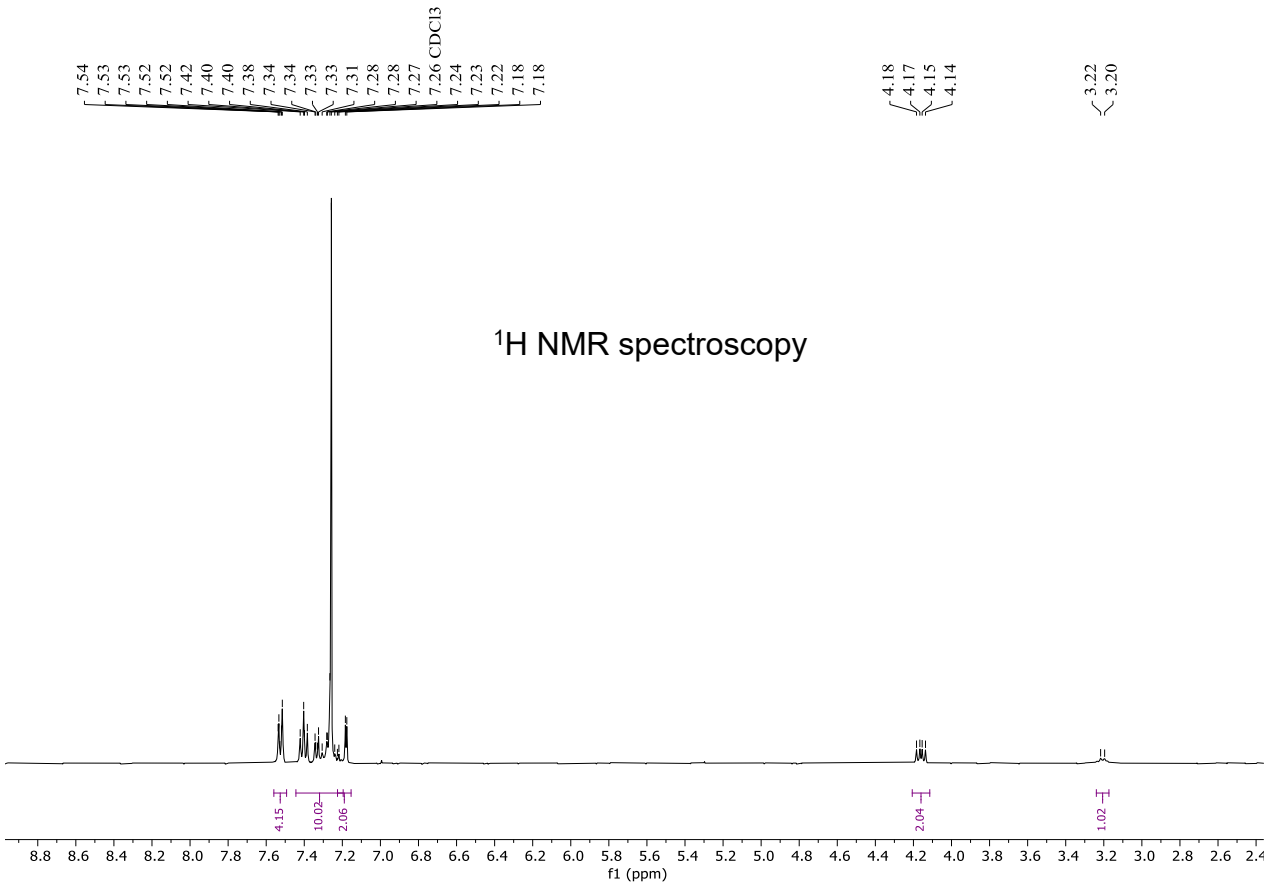

^{1}H NMR spectroscopy

^{13}C NMR spectroscopy

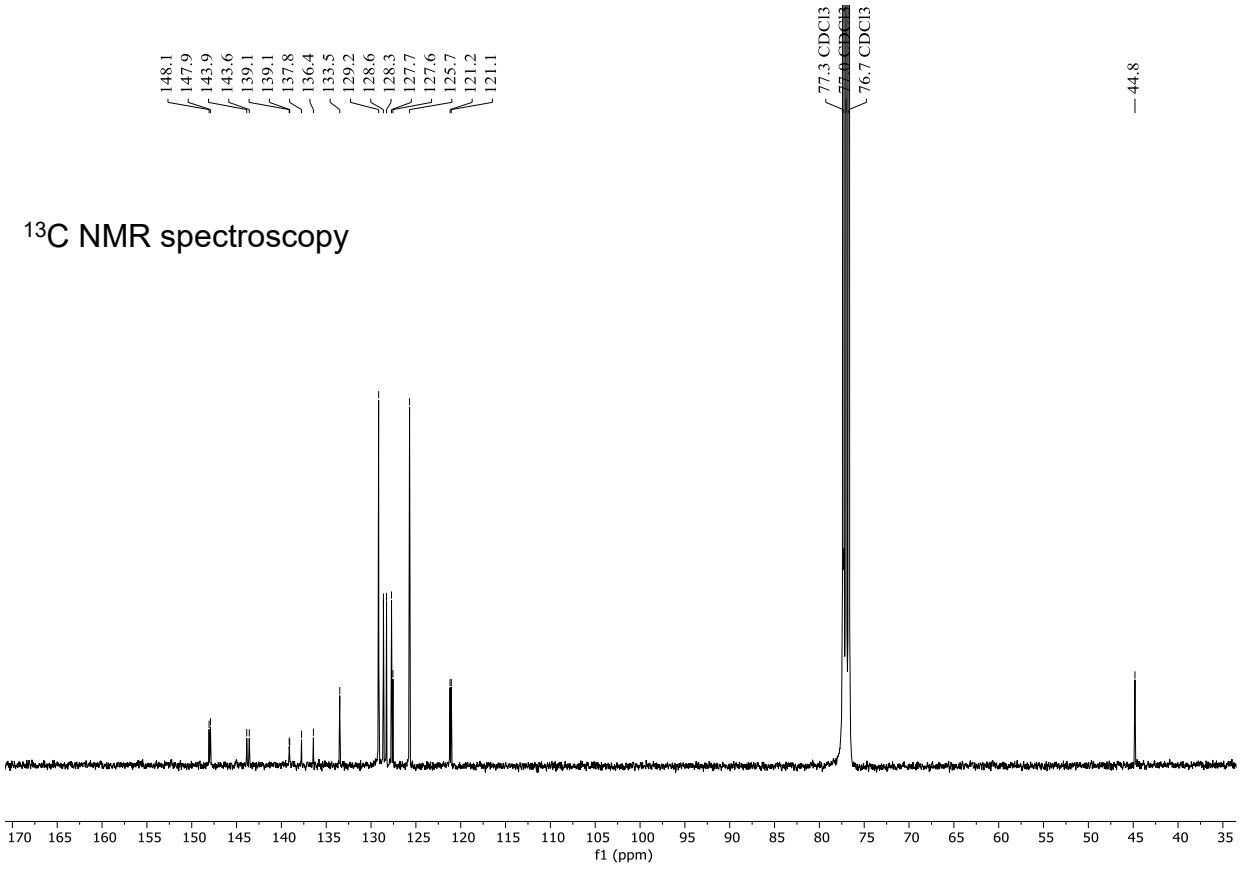

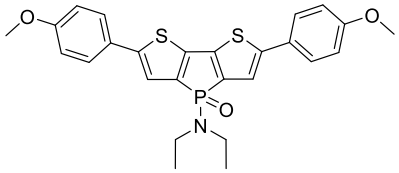

3-5

$^{31}P\{^{1}H\}$ NMR spectroscopy

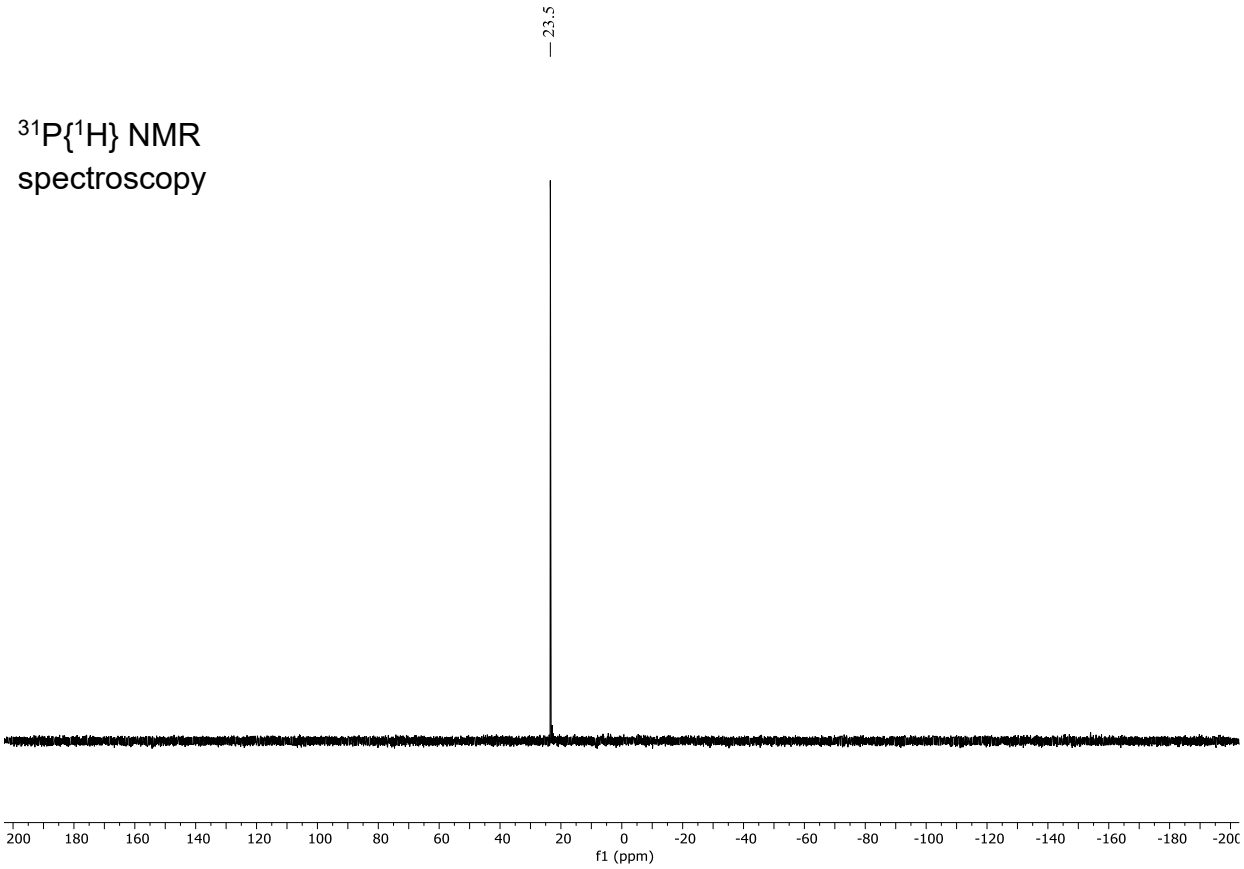

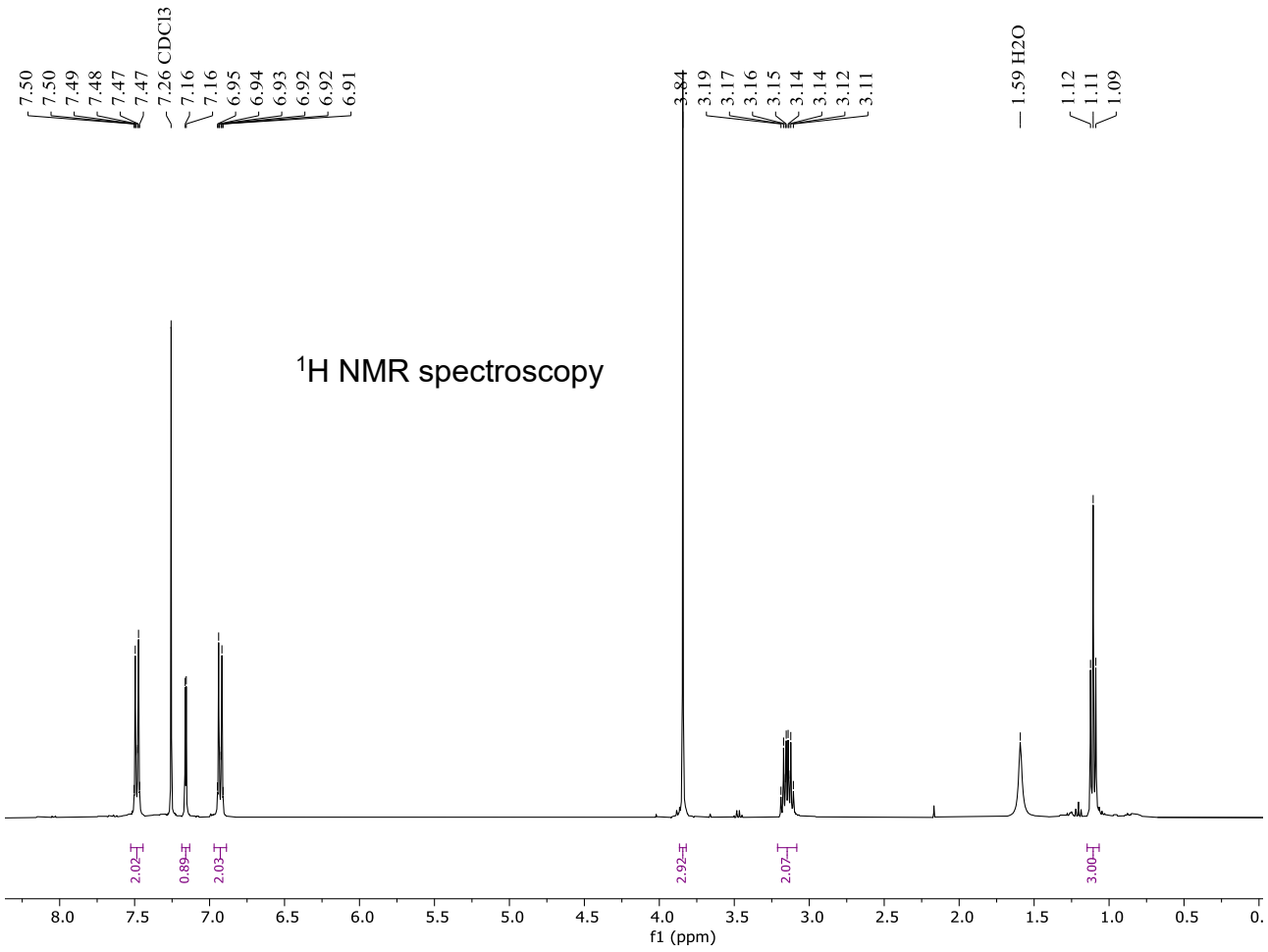
7.50
7.50
7.49
7.48
7.47
7.47
7.26 CDCl3
7.16
7.16
6.95
6.94
6.93
6.92
6.92
6.91
3.84
3.19
3.17
3.16
3.15
3.14
3.14
3.12
3.11
1.59 H2O
1.12
1.11
1.09
1H NMR spectroscopy
2.02
0.89
2.03
2.92
2.07
3.00
8.0
7.5
7.0
6.5
6.0
5.5
5.0
4.5
4.0
3.5
3.0
2.5
2.0
1.5
1.0
0.5
0.
f1 (ppm)

^{13}C NMR spectroscopy

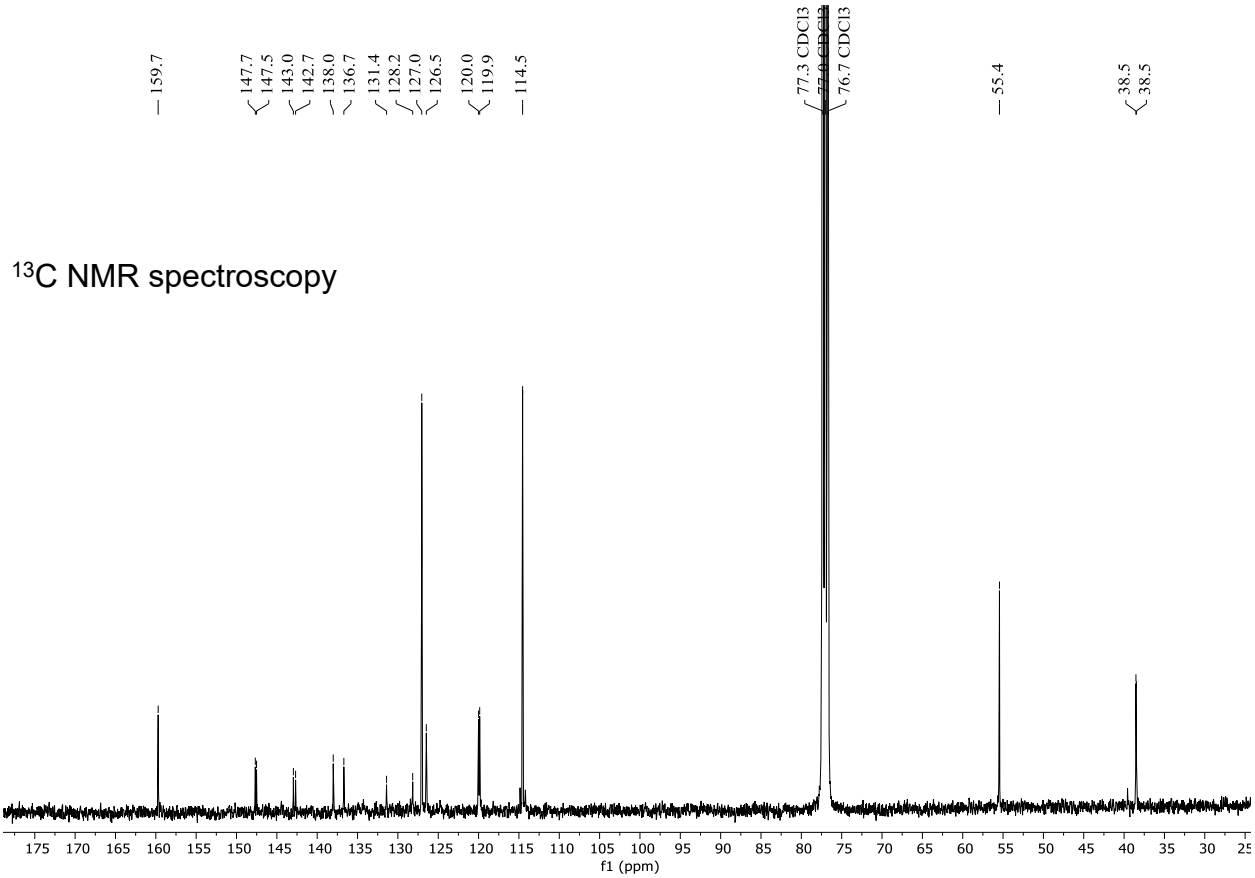

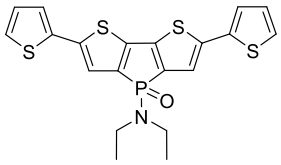

3-6

$^{31}P\{^{1}H\}$ NMR spectroscopy

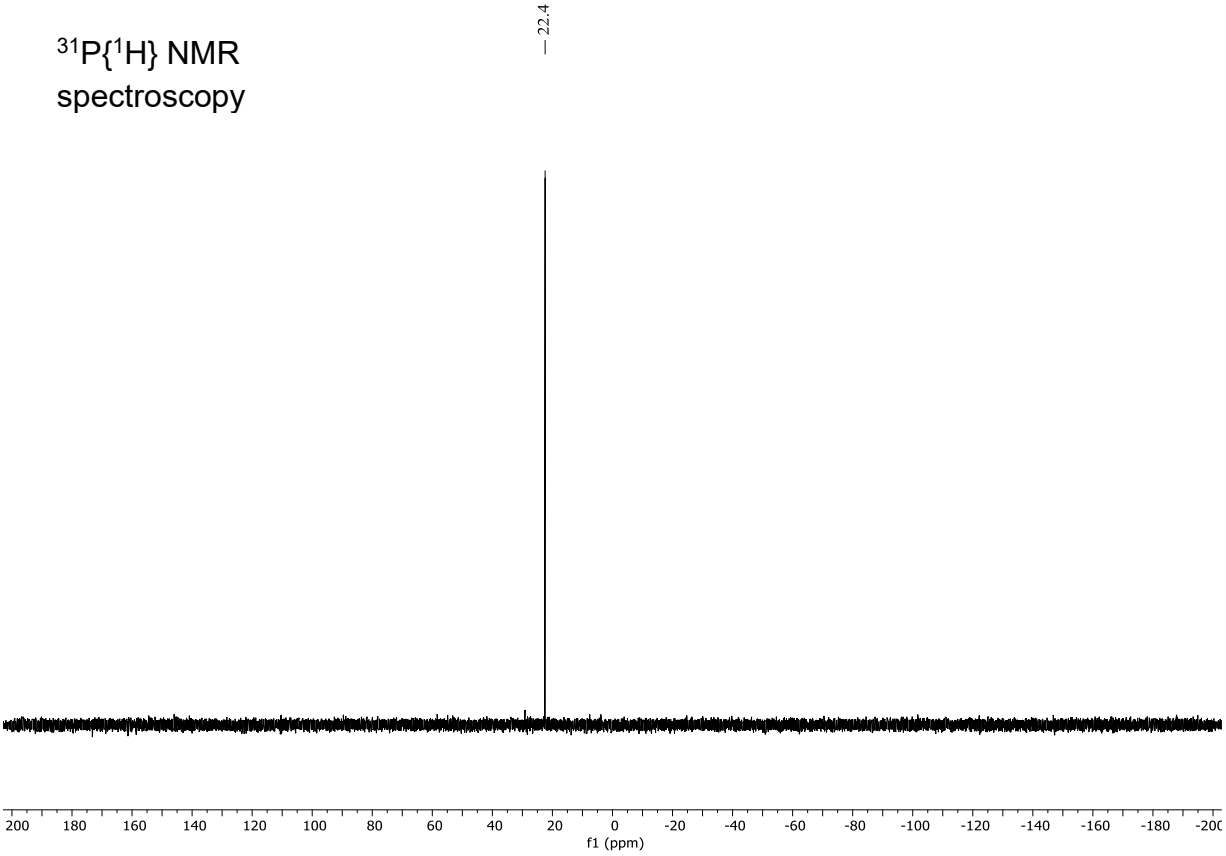

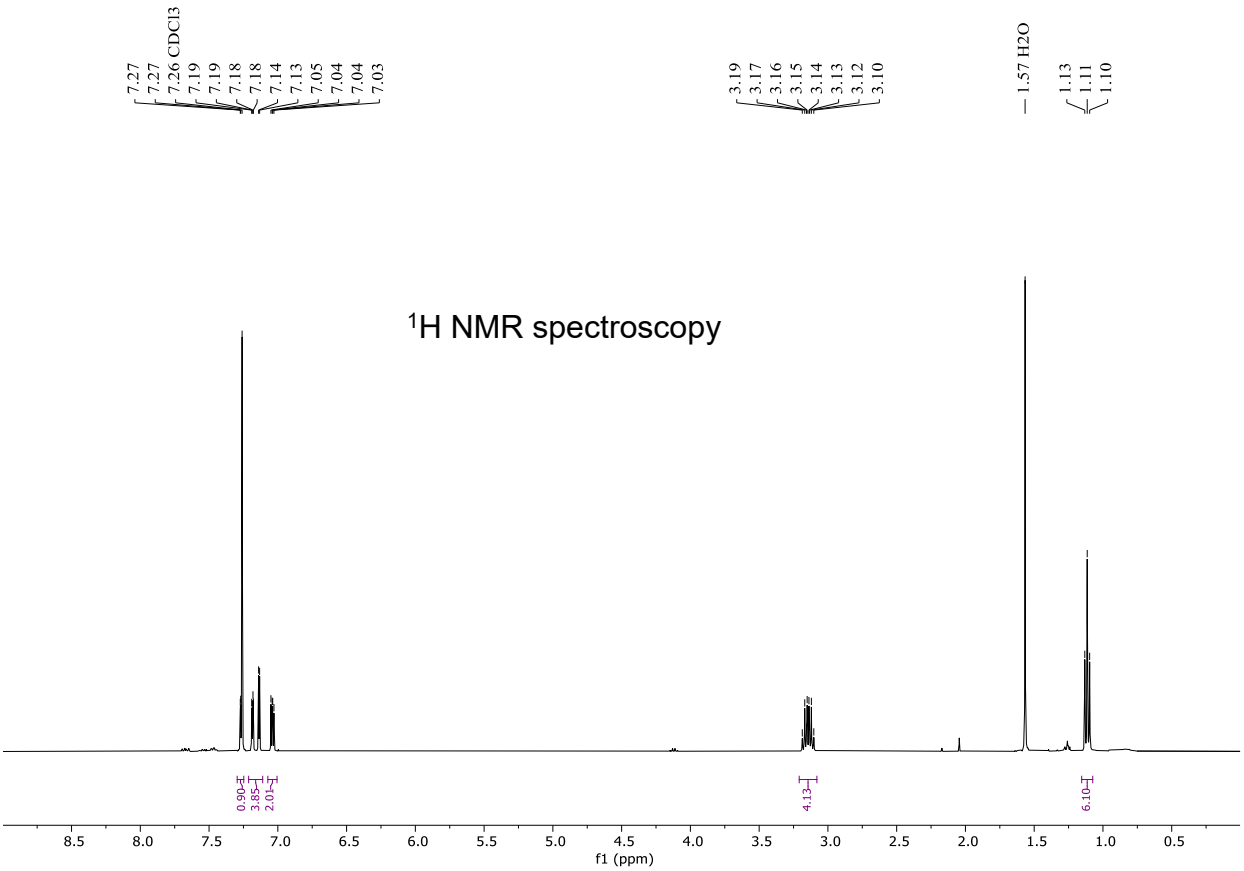

^{1}H NMR spectroscopy

^{13}C NMR spectroscopy